

**PONTIFICIA UNIVERSIDAD CATÓLICA DEL PERÚ**

**FACULTAD DE CIENCIAS E INGENIERÍA**



**Gamma-Hadron separation using the temporal distribution of particle  
cascades at TeV energies in the SWGO experiment**

**TESIS PARA OBTENER EL TÍTULO PROFESIONAL DE  
LICENCIADO EN FÍSICA**

**AUTOR:**

David Alonso Luzquiños Saavedra

**ASESOR:**

José Luis Bazo Alba


Lima, Mayo, 2024

### Informe de Similitud

Yo, .....José Luis Bazo Alba.....,  
docente de la Facultad de .....Ciencias e Ingeniería ..... de la Pontificia  
Universidad Católica del Perú, asesor de la tesis titulada  
.....Gamma-Hadron separation using the temporal distribution of particle cascades at TeV energies in  
the SWGO experiment.....,  
del autor .....David Alonso Luzquiños Saavedra.....,  
dejo constancia de lo siguiente:

- El mencionado documento tiene un índice de puntuación de similitud de 15%. Así lo consigna el reporte de similitud emitido por el software *Turnitin* el 13/05/2024.
- He revisado con detalle dicho reporte y la Tesis y no se advierte indicios de plagio.
- Las citas a otros autores y sus respectivas referencias cumplen con las pautas académicas.

Lugar y fecha: .....San Miguel, 13/05/2024.....

|  |   |
|--|---|
| Apellidos y nombres del asesor:<br><u>Bazo Alba, José Luis</u> |   |
| DNI: 41021164  | Firma<br> |
| ORCID: 0000-0001-9148-9101                                     |   |

## Resumen

Descubrir nuevas fuentes de rayos gamma de alta energía de origen galáctico (por ejemplo, en el centro galáctico o las Burbujas de Fermi) y extragaláctico (como cuásares o blazares) es de gran interés para la comunidad de física de astropartículas. Actualmente, los observatorios HAWC y LHAASO, ubicados en el hemisferio norte, utilizan detectores basados en el efecto Cherenkov en agua para detectar continuamente partículas secundarias de duchas atmosféricas iniciadas por rayos gamma primarios en la atmósfera. Dado que no existe un experimento equivalente en el hemisferio sur, el futuro observatorio de rayos gamma SWGO completará la cobertura del cielo para observatorios de alto ciclo de trabajo y campo de visión amplio. Su sitio propuesto por encima de los 4400 m estará ubicado en los Andes del Sur, con Chile, Argentina y Perú como países candidatos. El diseño de SWGO consiste en un arreglo de tanques de agua con dos núcleos circulares: el núcleo interno, alcanzando un radio de 160 m, con un 88% de área sensible y el anillo exterior, alcanzando un radio de 300 m, con un factor de llenado del 5%. Para identificar fuentes de rayos gamma, las partículas primarias deben reconstruirse a partir de las duchas aéreas que llegan al arreglo de detectores, obteniendo su energía, dirección y tipo. Un separador gamma/hadrón describe las características de las duchas aéreas para distinguir entre rayos gamma, considerados como señal, y hadrones (es decir, rayos cósmicos) que se consideran ruido. Esta tesis propone una variable alternativa de separador gamma/hadrón para distinguir entre tipos de duchas atmosféricas utilizando la distribución de tiempo de llegada de partículas secundarias a SWGO. Para definir la mejor nueva variable basada en el tiempo utilizamos el software CORSIKA para simular el desarrollo de la ducha aérea en la atmósfera hasta la llegada de las partículas secundarias al arreglo de tanques Cherenkov de agua. El análisis se realizó utilizando las condiciones geomagnéticas del sitio candidato de Imata en Arequipa, Perú, ubicado a 4500 metros sobre el nivel del mar. Consideramos como primarios fotones y protones con una trayectoria vertical en el centro del arreglo en el rango de energía de 1 a 100 TeV. El parámetro de separación óptimo encontrado es el tiempo para el percentil 15% de las partículas que llegan dentro de un anillo de 100 a 150 m. Tras el cálculo y la evaluación de la muestra de simulación, la señal reconocida es  $\gtrsim 88\%$  en promedio y el rechazo de fondo es ( $\gtrsim 90\%$ ). Ambos desempeños son comparables a usar la variable estándar de conteo de muones.

## Abstract

Discovering new sources of high energy gamma rays of galactic (e.g. in the galactic center or the Fermi Bubbles) and extragalactic origin (such as quasars or blazars) is of great interest to the astroparticle physics community. Currently the HAWC and LHAASO observatories, located in the Northern hemisphere, use detectors based on the Cherenkov effect in water to continuously detect secondary particles from atmospheric showers initiated by primary gamma rays in the atmosphere. Since there is no equivalent experiment in the Southern hemisphere, the future gamma-ray observatory SWGO will complete the sky coverage for high duty cycle and wide field of view observatories. Its proposed site above 4400 m will be located in the Southern Andes, with Chile, Argentina and Peru as candidate countries. The SWGO reference configuration consists of an array of water tanks with two circular cores: the inner core, reaching 160 m radius, with 88% sensitive area and the outer ring, reaching 300 m radius, with a 5% fill-factor. To identify gamma ray sources, primary particles need to be reconstructed from the air showers reaching the detector array, obtaining their energy, direction and type. A gamma/hadron separator describes the characteristics of the air showers to distinguish between gamma rays, considered as signal, and hadrons (i.e. cosmic rays) that are considered noise. This thesis proposes an alternative gamma/hadron separator variable to distinguish between types of atmospheric showers by using the arrival time distribution of secondary particles reaching SWGO. To define the best new time-based variable we use the CORSIKA software to simulate the development of air showers in the atmosphere up to the arrival of secondary particles at the array of water Cherenkov tanks. The analysis was done using the geomagnetic conditions of the Imata candidate site in Arequipa, Perú, located at 4500 meters above sea level. We considered as primaries photons and protons with a vertical trajectory in the center of the array in the energy range from 1 to 100 TeV. The optimal separation parameter found is the time for the 15% percentile of arriving particles inside a ring of 100 to 150 m. Following the calculation and evaluation of the simulation sample, the recognized signal is  $\gtrsim 88\%$  on average, and the background rejection is  $\gtrsim 90\%$ . Both performances are comparable to using the standard muon count variable.

## Agradecimientos

En primer lugar, quiero extender mi agradecimiento al CONCYTEC por financiar esta tesis como parte del Proyecto 078 – 2021 (Evaluación de Sitios Altoandinos en Perú para la Instalación del Futuro Observatorio de Rayos Gamma SWGO). Agradezco tanto con el equipo de SWGO-Perú como con el grupo de Altas Energías PUCP por su apoyo en la definición del tema, proporcionándome orientación desde el comienzo de la idea principal. Estoy profundamente agradecido con mi asesor José Bazo por su constante apoyo con todas las consultas que surgieron, gracias por siempre darme tiempo para esas extensas discusiones sobre lo que podría mejorarse en este trabajo. Asimismo, agradezco a mis amigos: Luis Morales quien me apoyó considerablemente en el proceso de instalación de los simuladores y Andrés Colán por su gran apoyo en la optimización de los algoritmos y su desinteresada asistencia; sin ti, no podría haberlo logrado, eres un gran amigo. Finalmente, agradezco a mi madre, Magaly Saavedra, y hermanito, Ismael Luzquiños, quienes me acompañaron durante todo el proceso, desde las mañanas cuando me traían un cálido desayuno hasta las largas noches en las que, preocupados, me preguntaban cómo iba y cuándo iba a descansar. Agradezco a mi pareja, Adriana Herrera, por siempre darme ánimos y fuerzas en los momentos más difíciles de este largo viaje. No quiero terminar estas palabras sin mencionar a cada familiar y amigo que me aportó un aliento o idea a lo largo del desarrollo de esta investigación. Fui muy afortunado de tenerlos a todos, sin alguno de ustedes, esta investigación no habría sido posible.

Muchas gracias.

## **Acknowledgement**

Firstly, I want to extend my gratitude to CONCYTEC for funding this thesis as part of Project 078 – 2021 (Evaluation of High-Andean Sites in Peru for the Installation of the Future SWGO Gamma Ray Observatory). I am grateful to both the SWGO-Peru team and the PUCP High Energy group for their support in defining the topic, providing me with guidance from the very start of the main idea. I am deeply thankful to my advisor José Bazo for his constant support with all the queries that arose, thank you for always making time for those extensive discussions about what could be improved in this work. Likewise, I am grateful to my friends: Luis Morales, who supported me considerably in the process of installing the simulators, and Andrés Colán for his great support in optimizing the algorithms and his selfless assistance; without you, I could not have achieved it, you are a great friend. Finally, I thank my mother, Magaly Saavedra, and little brother, Ismael Luzquiños, who accompanied me throughout the entire process, from the mornings when they brought me a warm breakfast to the long nights when they, worried, asked me how it was going and when I was going to rest. I thank my partner, Adriana Herrera, for always giving me encouragement and strength during the most difficult moments of this long journey. I do not want to end these words without mentioning every family member and friend who provided encouragement or ideas throughout the development of this research. I was very fortunate to have all of you; without any one of you, this research would not have been possible. Thank you very much.



To Ismael Luzquiños, my beloved little brother.

# Contents

|          |   |          |
|----------|---|----------|
| <b>1</b> | <b>Introduction</b>   | <b>1</b> |
| <b>2</b> | <b>Gamma Astronomy</b>  | <b>3</b> |
| 2.1      | Types of Cosmic Radiation   | 3        |
| 2.1.1    | Cosmic Rays   | 3        |
| 2.1.2    | Gamma Rays  | 4        |
| 2.2      | Sources of Cosmic Radiation   | 4        |
| 2.2.1    | Galactic Sources  | 5        |
| 2.2.2    | Extragalactic Sources   | 6        |
| <b>3</b> | <b>Active Galactic Nuclei (AGN)</b>   | <b>7</b> |
| 3.1      | Brief history of AGNs   | 7        |
| 3.2      | What is an AGN?   | 8        |
| 3.3      | Components  | 8        |
| 3.3.1    | Black Hole  | 8        |
| 3.3.2    | Accretion Disk - Dust Torus   | 9        |
| 3.3.3    | Line Emitting Regions   | 10       |
| 3.3.4    | Jets  | 10       |
| 3.4      | Characteristics   | 11       |
| 3.5      | Unified Model   | 11       |
| 3.5.1    | First classification: Radio Emission  | 11       |
| 3.5.2    | Second classification: Orientation and characteristics in the optical and<br>UV | 12       |
| 3.6      | Blazars   | 13       |



# CONTENTS

|          |  |           |
|----------|--|-----------|
| 3.6.1    | Variability . . . . .  | 14        |
| 3.6.2    | Relativistic Jets . . . . .  | 14        |
| <b>4</b> | <b>Particle Interactions</b>                                       | <b>16</b> |
| 4.1      | Atmospheric Air Showers . . . . .                                  | 16        |
| 4.1.1    | Gamma rays as primary particles . . . . .                          | 17        |
| 4.1.2    | Hadrons as primary particles . . . . .                             | 19        |
| 4.2      | Cherenkov Effect . . . . .   | 20        |
| 4.2.1    | Air Cherenkov effect . . . . .                                     | 21        |
| 4.2.2    | Water Cherenkov effect . . . . .                                   | 23        |
| <b>5</b> | <b>The Southern Wide-field Gamma-ray Observatory (SWGGO)</b>       | <b>24</b> |
| 5.1      | Specifications . . . . .   | 24        |
| 5.2      | Science Case . . . . .   | 27        |
| 5.2.1    | Blazars observable in the Southern hemisphere (by SWGGO) . . . . . | 28        |
| 5.3      | Site Candidates . . . . .  | 30        |
| 5.3.1    | Peruvian candidates . . . . .                                      | 31        |
| 5.3.2    | Other candidates . . . . .   | 32        |
| 5.3.3    | Assembly Process of a Cherenkov Tank in Peru . . . . .             | 33        |
| <b>6</b> | <b>Simulations using CORSIKA</b>                                   | <b>35</b> |
| 6.1      | CORSIKA Simulations . . . . .                                      | 35        |
| 6.2      | Simulation of the SWGGO configuration . . . . .                    | 37        |
| 6.2.1    | Study by Concentric Rings . . . . .                                | 37        |
| <b>7</b> | <b>Air Showers Reconstruction</b>                                  | <b>39</b> |
| 7.1      | Core Location Reconstruction . . . . .                             | 39        |
| 7.2      | Direction Reconstruction . . . . .                                 | 40        |
| 7.3      | Energy Reconstruction . . . . .                                    | 41        |
| 7.4      | Gamma-Hadron Separation . . . . .                                  | 41        |
| 7.4.1    | Muon Count . . . . .   | 42        |

|           |   |           |
|-----------|---|-----------|
| 7.4.2     | Compactness.....  | 44        |
| 7.4.3     | PINCESS (Parameter for Identifying Cosmic rays).....                                    | 45        |
| 7.4.4     | LIC (Logarithm of Inverse Compactness) .....  | 45        |
| 7.4.5     | disMax (Maximum Distance between PMTs) .....  | 46        |
| <b>8</b>  | <b>Air Showers Temporal Distribution</b>  | <b>47</b> |
| 8.1       | Analysis of the Temporal Distribution.....  | 47        |
| 8.1.1     | Quantiles of the Temporal Distribution .....  | 48        |
| 8.2       | Candidates for Temporal Gamma Hadron Separation .....                                   | 52        |
| 8.2.1     | Limiting the Optimal Rings .....  | 52        |
| 8.2.2     | Searching for Time Quantile Trends in Rings .....                                       | 52        |
| <b>9</b>  | <b>Evaluating the Time Gamma/Hadron Separator</b>                                       | <b>56</b> |
| 9.1       | Calculation and Evaluation of the Time Variable.....                                    | 56        |
| 9.1.1     | Evaluating of the Muon Count Variable in SWGO.....                                      | 59        |
| 9.2       | Results of the Comparison between the time cut separator and the Reference<br>(MC)..... | 60        |
| <b>10</b> | <b>Conclusions</b>  | <b>63</b> |
| <b>11</b> | <b>Bibliography</b>   | <b>65</b> |

# Chapter 1

## Introduction

Humans, since their beginnings, have looked at the sky with great wonder, questioning their place in the universe. This journey has taken them from the discovery of fire to the creation of colossal particle accelerators. It is in this context that the exploration of the night sky has served as a stage for the search for new physics through the study of celestial bodies located in the vicinity of the cosmos. The study of the sky in the gamma spectrum has been of interest for the exploration of the observable universe and the origin of cosmic radiation from both galactic and extragalactic sources.

This thesis will detail, in Chapter 2, the types of cosmic radiation, with a particular focus on galactic and extragalactic astrophysical sources, especially Active Galactic Nuclei. One of the most prominent types of extragalactic sources are Active Galactic Nuclei, described in Chapter 3, among which blazars stand out for having a relativistic jet of particles pointing towards the Earth.

When a gamma ray, or a cosmic ray, approaches the Earth and interacts with its atmosphere colliding with, for example, an ozone nucleus, it produces the first secondary particles, later generating more particles forming a chain event called air shower, described in Chapter 4. In this context, the study of air showers generated by gamma rays emitted from these sources is crucial in particle astrophysics to understand their emitters. In this part we also focus on their detection methods (Cherenkov effect in air and water).

Observatories such as HAWC and LHAASO are responsible for detecting these events in the Northern hemisphere with vast arrays of water-filled tanks, with a PMT that is used for the detection of Cherenkov light produced by the secondary particles generated by the air showers.

## CHAPTER 1. INTRODUCTION

Such a detector does not yet exist in the Southern Hemisphere, so an observatory based on ground-based water tank units located in Southern latitudes, specifically in the South American Andes called the Southern Wide-field Gamma-ray Observatory (SWGGO) is proposed and will be described in Chapter 5. SWGGO will be able to observe the sky in the gamma spectrum covering energies from hundreds of GeV's to the order of PeV with a wide field of view.

To study both the propagation of these events and their interaction with the detectors and their detection as such, it is necessary to carry out simulations in different types of programs such as CORSIKA, which emulates the propagation of the air shower or AERIE which, based on the CERN GEANT4 package, emulates the interaction between secondary particles and the tank distribution. The air shower simulation for SWGGO are introduced in Chapter 6.

Based on the data provided by the simulators or by the detector array post-event detection, it is necessary to use algorithms for the reconstruction of both the properties of the air shower and the primary particle that initiated it. This thesis, in Chapter 7, will cover some of the most important methods for reconstructing these properties such as Core Location, Direction Reconstruction, Energy Reconstruction and will focus on the variables that are based on the algorithm that distinguishes between air showers initiated by gamma rays, considered signal, and those initiated by cosmic rays, considered as noise called Gamma/Hadron Separation.

The focus of this thesis lies in the search for a new gamma/hadron separation variable based on the time distribution of secondary particles that can distinguish hadronic from gamma air showers, described in Chapter 8. For this purpose, simulations using photons and protons covering energies from 1 to 100 TeV, with the geomagnetic specifications (altitude and magnetic field) of Imata-Arequipa, are carried out. The temporal distributions are analyzed by geometric sectors, using rings that increase their radii by 50 m and temporal sectors, using time quantiles; with the purpose of finding the optimal candidate for gamma-hadron separator. In Chapter 9, a evaluation is performed with the optimal variable, obtaining an average recognized signal and an average noise rejection at all energies under analysis. Finally, in Chapter 10, the conclusions and limitations of this work are given.

# Chapter 2

## Gamma Astronomy

Conventional astronomy observes the cosmos in a narrow spectrum limited by the light (radiations) that the human eye can see. However, there are bodies that emit in other spectra of light invisible to the human eye [1]. From the idea of observing the cosmos in other regions of the electromagnetic spectrum, the exploration of the sky in the infrared, microwave, among others, began.

### 2.1 Types of Cosmic Radiation

In the observable universe, violent astrophysical phenomena occur that result in the emission of highly energetic radiation, such as gamma rays, which in various stellar and interstellar scenarios can span energies from Mega-electronvolts (MeV) to, according to the latest observations, exceeding Peta-electronvolts (PeV) [2]. In addition to gamma radiation, the production of these events generates other types of cosmic radiation, including protons, electrons, and heavy atomic nuclei, among others.

#### 2.1.1 Cosmic Rays

Cosmic ray particles are ionized nuclei, electrons, or positrons, composed of about 90% protons, 9% alpha particles, and the rest heavier nuclei. They are distinguished by their high energies, with most being ultra-relativistic. Due to their charge, cosmic rays deviate from their trajectory (momentum) while interacting with magnetic fields (e.g., the source's field) along their path from the source to the Earth's atmosphere (see Fig.2.1) [3]. Cosmic rays cannot provide information about the direction of their source due to the deflection they undergo in their tra-

## CHAPTER 2. GAMMA ASTRONOMY

jectory. Therefore, the origin of cosmic rays remains an open question in astroparticle physics. It is worth mentioning that cosmic rays of the highest energies could provide such information; however, in the range of energies studied in this work (from 1 to 100 TeV), cosmic rays will be considered as background. This is because one of the motivations of gamma-ray astronomy is to receive information from observed galactic or extragalactic sources emitting the detected radiation.

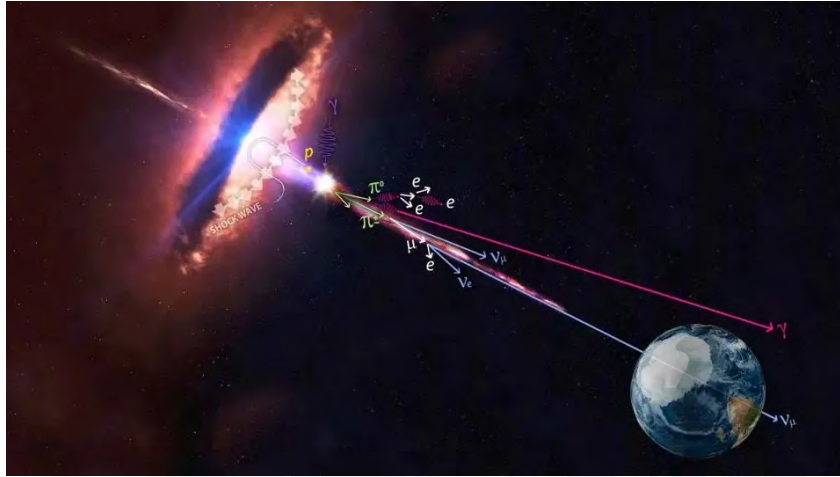


**Figure 2.1:** A blazar, whose relativistic particle jet (a beam pointing towards Earth) emits various types of cosmic radiation, cosmic rays (e.g., protons) are deflected by electromagnetic fields, whereas gamma rays and neutrinos (chargeless particles) maintain their direction due to their neutral nature[4]. Credit: IceCube/NASA

### 2.1.2 Gamma Rays

Gamma rays are highly energetic photons that can reach energies up to the PeV range. Being electrically uncharged particles, they do not interact with electromagnetic fields (see Fig. 2.1) that lie between the source and the Earth's atmosphere. Therefore, when observed, they can provide information about the direction in which the source is located.

Another type of particle with this characteristic are neutrinos, which, like gamma rays lack electric charge. However, they are more challenging to detect due to their interaction type (weak nuclear force).

## 2.2 Sources of Cosmic Radiation

The sources of cosmic rays can be divided into two types:

## CHAPTER 2. GAMMA ASTRONOMY

**Galactic Sources:** those found within the Milky Way, of particular interest due to their proximity to Earth.

**Extragalactic Sources:** those occurring outside our galaxy, encompassing energies surpassing the former.

### 2.2.1 Galactic Sources

Galactic sources are celestial bodies or systems located within the Milky Way that produce astrophysical events emitting, among other things, gamma rays[5]. Some of these sources include supernova remnants (Type Ia, Ib/c, or Type II), X-ray binaries (LMXB or HMXB), pulsars (gamma-ray and magnetars) and the galactic center. The galactic center has a supermassive black hole Sagittarius A, along with a high concentration of massive stars and other celestial bodies of interest (see the center of Fig.2.2 where there is high luminosity due to this concentration), which can be gamma-ray emitters [5]. Some of the highly interesting sources include the Fermi Bubbles, which are two large emission lobes (see Fig.2.2) extending nearly 10 kpc in diameter to the North and South of the galactic center [6]. Although these bubbles were detected by the Fermi Large Area Telescope in 2010 and there are some possible explanations about their nature and origin, these are still uncertain [6].

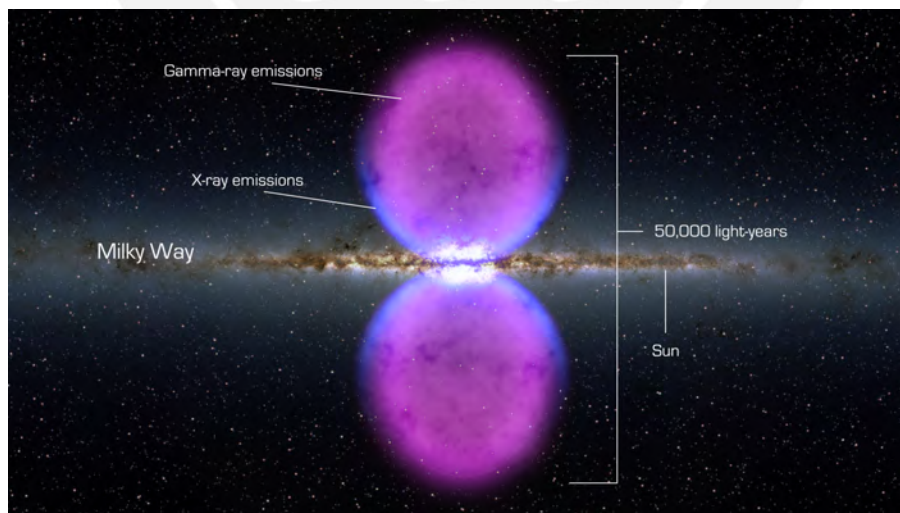


**Figure 2.2:** Side view of the Milky Way with the Fermi Bubbles, gamma-ray emitters, depicted in pink along with their extent, and the location of the Solar System on the right[7]. Credit: NASA's Goddard Space Flight Center.

## CHAPTER 2. GAMMA ASTRONOMY

### 2.2.2 Extragalactic Sources

Extragalactic sources refer to objects or systems that emit radiation beyond the boundaries of the Milky Way. Similar to galactic sources, they generate events that can emit cosmic rays and gamma rays, but unlike galactic sources, they have higher energies. Among them are Active Galactic Nuclei (AGN), including blazars, quasars, and other AGN, as well as stellar and non-stellar black holes, extragalactic pulsars, galaxy clusters, gamma-ray bursts (GRB), and others [8]. In this work, we will delve into blazars since they emit particles (relativistic jets) directed towards Earth (see Fig.2.1).





# Chapter 3

## Active Galactic Nuclei (AGN)

This chapter will provide a brief description and classification of the different AGN, and will then focus on AGNs whose relativistic jets are pointed towards Earth, known as blazars. This is motivated because the future gamma-ray experiment SWGO will observe, among other important sources, blazars located in the observable zone from the Southern Hemisphere.

### 3.1 Brief history of AGNs

The 20th century witnessed the discovery of new non-stellar sources. Until then, the electromagnetic radiation emitted by common (non-active) galaxies was produced by the thermal emission of the stars (sources) that make them up, with a peak emission frequency around  $10^{14}$  Hz due to the superposition of the individual Planck spectra of the sources [9]. However, research began in the early 20th century that would reveal a different form of emission.

In 1908, while examining the galaxy NGC 1068 at the Lick Observatory by E.A. Fath, strong emission lines were identified with line widths greater than 3000 km/s [10]. Later, in 1943, Carl Seyfert [11] conducted a systematic analysis of galaxies, selecting those that exhibited such features (based on their high brightness), being the first to realize that there are several similar galaxies that form a distinct class [12], thus drawing astronomers' attention to this new category [10].

Seyfert discovered that the optical spectra of several of the galaxies he analyzed are dominated by high-excitation nuclear emission lines whose most important characteristics are: (1) Broad emission lines (up to 8500 km/s). (2) Some hydrogen lines are broader than the other lines. Seyfert-type galaxies did not receive much attention until the 1960s [12] when galaxies of this

## CHAPTER 3. ACTIVE GALACTIC NUCLEI (AGN)

type (NGC 1068 & NGC 1275), based on observations at 158MHz, were detected as a source of radio emission, later termed quasi-stellar radio sources or quasars [9].

In 1963, Martín Schmidt analyzed the redshift of the radio source 3C 273 and showed that it is a very powerful and distant galaxy. In addition, optical observations revealed that light emission mainly comes from the center of the galaxy, being so bright that it overshadows the surrounding stars [9]. For this last characteristic, these galaxies are called AGN.

### 3.2 What is an AGN?

AGNs are objects, located at the center of a galaxy, that produce extremely high luminosity (in some cases they can apparently reach a thousand times the luminosity of a typical galaxy) in very small spaces. The radiations they emit can arise in a very wide range of frequencies and their nature, unlike common galaxies, arises from non-thermal processes: the accretion (gravitational) of matter towards their center where there is a supermassive black hole (hereinafter SMBH) [13].

### 3.3 Components

All types of AGN have certain common components. The following will detail the parts of these extragalactic sources and discuss the effects they produce, such as matter accretion, particle acceleration, among others.

#### 3.3.1 Black Hole

From the spectroscopic observations conducted on the gas disk within the nucleus of the M87 galaxy found by [15], [16] reported evidence of the presence of a strong gravitational source in the central region causing rapid rotation in the gaseous disk. From this study, an estimated SMBH mass of  $(2.4 \pm 0.7) \times 10^9 M_{\odot}$  (solar masses) was obtained.

Years later, more convincing evidence of the SMBH presence was obtained using the Very Long Baseline Array (VLBI) technique [17], analyzing the LINER galaxy NGC 4258. It was determined with great precision that the central mass was  $(3.8 \pm 0.1) \times 10^7 M_{\odot}$ , confined within a very small radius of approximately  $\sim 0.1$  pc. It cannot be anything else but a SMBH [18].

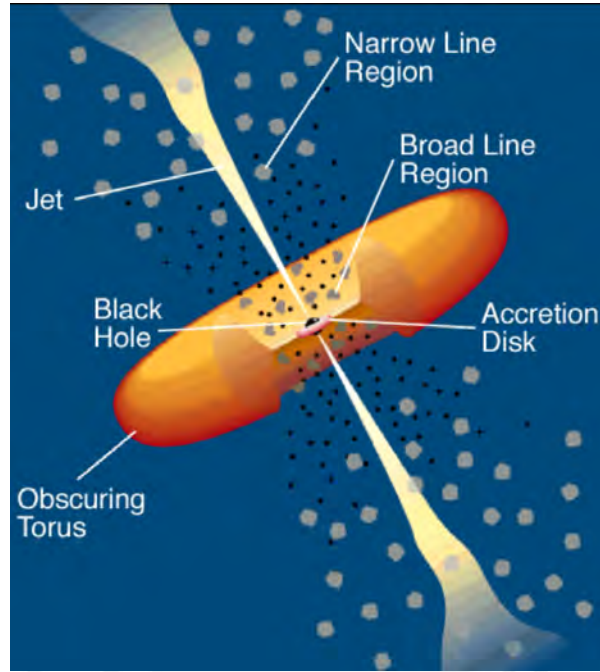


**Figure 3.1:** A diagram of the components of a radio-loud AGN (not to scale). A brilliant accretion disk surrounds the central region where a supermassive black hole (SMBH) is located. The broad emission lines originate from clouds orbiting around the disk, possibly even within the disk itself. A dense and dusty torus (or inclined disk) acts as a screen that conceals the region where the broad lines are situated when observed from a perpendicular angle. Some of the components of the continuum and broad-line emission may scatter into these lines of sight due to the presence of hot electrons in the region [14].

In 2019, through experiments conducted with the Event Horizon Telescope (EHT), it was possible to directly observe the surrounding area of the black hole in the Messier 87 galaxy, thereby demonstrating the presence of a black hole [19].

The previous contributions are just some of the various pieces of evidence that the centers of galaxies (non-active) and, especially, AGNs, host SMBHs (see Fig.3.1 with masses that can reach on the order of  $10^9 M_{\odot}$  [20]. Its presence explains the energy emanating from the AGN through gravitational potential via matter accretion.

Furthermore, the rapid variability of its luminosity, which can vary by 50% on timescales of days, can be explained by the small volume of the emitting regions, which is related to the size of the SMBH ( $R \lesssim 1 \text{ lightday} \sim 3 \times 10^{15} \text{ cm}$ ) [18].

### 3.3.2 Accretion Disk - Dust Torus

The accretion processes in the vicinity of the SMBH lead to the influx of gas, likely non-uniformly, resulting in gravitationally captured gas carrying net angular momentum [21].

## CHAPTER 3. ACTIVE GALACTIC NUCLEI (AGN)

In such a scenario, the centrifugal force will impede accretion around the circulation radius ( $r_{\text{circ}} \approx \frac{l^2}{2GM}$ , where  $l$  denotes angular momentum per unit mass). This leads to the formation of a rotationally supported configuration in the form of a disk or dust torus (see Fig.3.1). To sustain the accretion process, a portion of the trapped gas (internal) within the accretion disk (or dust torus) must shed angular momentum, causing it to move inwards, while the outer regions gain angular momentum and move outwards [21].

### 3.3.3 Line Emitting Regions

AGNs are composed of regions (see Fig.3.1) that emit different types of emission spectra (broad and narrow), from which properties of the AGN itself can be studied. Below is a summary of the characteristics of these zones and the properties that can be determined from their respective study in Table 3.1.

| Type of Lines          | Broad Lines   | Narrow Lines  |
|------------------------|---|---|
| Order                  | $10^3$ Km/s [22]  | $10^2$ Km/s [22]  |
| Regions                | Regions of matter close to the central black hole [22]    | Regions of matter farther from the central black hole [22]                        |
| Distance to the center | From 2 to $20 \times 10^{16}$ cm close to the center [22] | From $10^{18}$ to $10^{20}$ cm close to the center and with lower velocities [22] |

**Table 3.1:** Summary of characteristics of the regions that emit broad and narrow lines [22], and the AGN properties [14] that can be determined based on [5].

### 3.3.4 Jets

During the process of accretion, there is the creation of highly focused and collimated outflows that have a bipolar nature, commonly referred to as jets [9]. There are bipolar flow emanations at the center of the AGN that form a  $90^\circ$  angle with respect to the plane of the SMBH's accretion disk and are primarily composed of relativistic matter and high-energy photons (soft X-rays up to violent  $\sim$  TeV gamma rays) [5]. They can be observed on scales from  $10^{17}$  to  $10^{24}$  cm [14].

### 3.4 Characteristics

Some distinctive characteristics of AGNs that set them apart from ordinary (non-active) galaxies include the following:

- **High Luminosity (strong emission):** Reaching luminosities exceeding those of “ordinary” galaxies by  $10^4$  times. It is accepted that this characteristic is due to matter accumulating towards, and falling into, a SMBH [23].
- **Broadening and narrowing of emission lines:** The cause is due to Doppler broadening, when a source (AGN) is approaching the observer (on Earth), the lines tend to have a blue shift, and if on the contrary, it moves away, they present a red shift. At higher speeds, Doppler effects are more noticeable, which makes the emission/absorption lines broader.[5]

### 3.5 Unified Model

The Unified Model of AGNs[14] proposes that all AGNs have the same composition: a supermassive black hole (SMBH) at their center, surrounded by an accretion disk of matter, and around it, a toroidal dust surface is formed. The difference lies mainly in the orientation between the source (AGN) and the observer, who is naturally located on Earth (see Fig. 3.2). Specifically, reference is made to the angle formed by the jet of relativistic particles with the observer’s line of sight (which is drawn from the observer to the location of the source) [24].

As seen in Fig. 3.2, depending on the relative orientation between the observer and the source direction (specifically the jet), one or another type of AGN is observed (e.g. when the angle between the observer and the jet direction is very small, blazars will be observed).

Historically, orientation relative to the observer has not been the sole factor for differentiating AGNs. Two main classifications will be detailed below.

#### 3.5.1 First classification: Radio Emission

The type of galaxy that contains the AGN is related to its radio frequency emission, specifically, under this variable, we can distinguish between two types of galaxies: those that emit radio

## CHAPTER 3. ACTIVE GALACTIC NUCLEI (AGN)

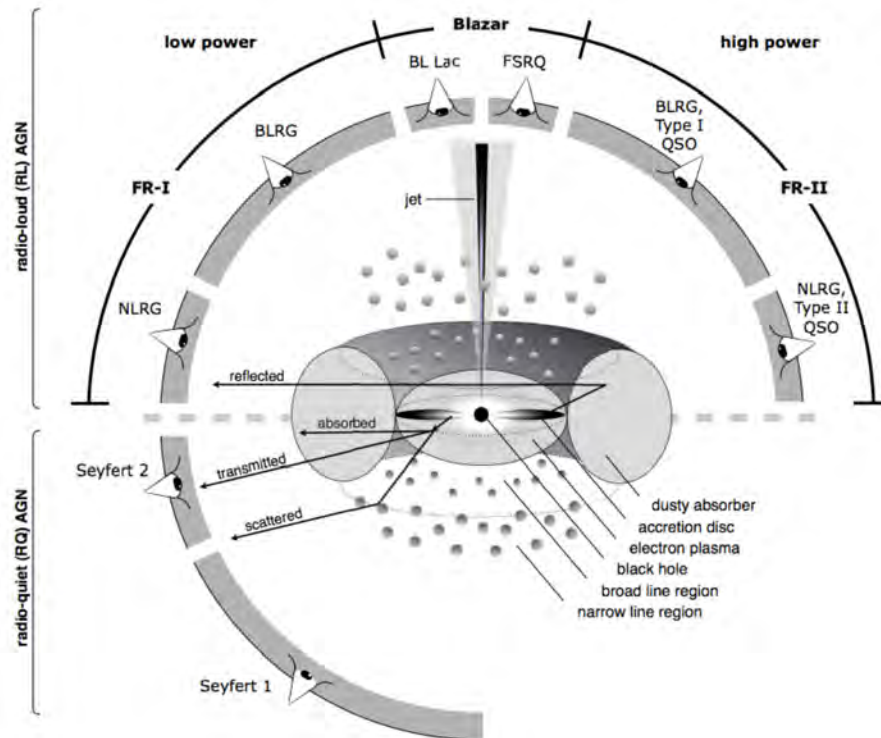


**Figure 3.2:** Unified Model of AGNs: the relative angle formed between the jet of particles and the observer defines the type of observed source (AGN) [14].

frequencies (radio loud) and those that do not (radio quiet) [5].

The general characteristics, associated galaxy type, estimated quantity, and environment or density of each type of galaxy can be observed in Table 3.2.

### 3.5.2 Second classification: Orientation and characteristics in the optical and UV

The classification proposed by [14] will be detailed below, which takes into account, among other factors, the orientation between the source (AGN) and the observer (naturally on Earth).

- Type 1
  - They are AGNs that have broad lines in the emission spectrum, which originate from matter accreting onto the supermassive black hole.
- Type 2
  - They are AGNs that have narrow emission lines in the emission spectrum. In these AGNs, the accreting material does not move very fast (it is farther from the super-

### CHAPTER 3. ACTIVE GALACTIC NUCLEI (AGN)

| Emission Type           | Radio Loud   | Radio Quiet   |
|-------------------------|--|---|
| General Characteristics | Produce large-scale jets and lobes with strong radio emission, and the luminosity of the jet contributes a significant fraction to the total luminosity of the source. | They are not as luminous. They do not contribute significantly to the total luminosity of the source. |
| Associated Galaxy Type  | They are associated with elliptical galaxies   | They are associated with spiral galaxies  |
| Estimated Quantity      | 85 to 95% of AGNs  | -   |
| Environment or Density  | The environment or density they inhabit is 10 times lower than that of the radio quiet.  | -   |

**Table 3.2:** Classification of AGNs by their emission in radio frequencies [5].

massive black hole, resulting in lower gravitational attraction). Additionally, this material is obscured by the toroidal structure, which absorbs the generated emissions.

- Type 0
  - There is only a small observed quantity of these AGNs. They have emission spectra different from those of the two previous types and do not exhibit emission lines, or if they do, they are very narrow.

Taking into account both classifications, the unified model of AGNs would ultimately propose Table 3.3, allowing for a more detailed classification of these sources.

|             | Type 2                         | Type 1               | Type 0                         |
|-------------|--------------------------------|----------------------|--------------------------------|
| Radio Quiet | Seyfert 2                      | Seyfert 2<br>QSO     |                                |
| Radio Loud  | NLRG:<br>• F.R. I<br>• F.R. II | BLRG<br>SSRQ<br>FSRQ | BLAZARS:<br>• BL Lac<br>• FSRQ |

**Table 3.3:** Classification of AGNs with the Unified Model [14].

## 3.6 Blazars

Blazars (BL Lac & FSRQ) are AGNs whose relativistic particle jet makes an angle close to zero with observer's line of sight [25]. Some of the most important characteristics of blazars will be

described below:

### 3.6.1 Variability

Observations made on different blazars suggest that they exhibit rapid flux variability [26] at all wavelengths on different time scales: intra-day (IDV), short-term (STV), and long-term (LTV) [27]. That is, these time scales can range from minutes (e.g., Markarian 421: 15 minutes [28]) to months [5].

General constraints on the emission mechanism can be derived from these variations, providing insights into the structure of the source [27]. One important characteristic that can be discerned from the variability is the size of the emitting region, since rapid variability suggests a very compact gamma-ray emitting region [29].

Equation 3.1 provides an upper limit to the radius of the emitting region:

$$R \leq \frac{\delta c \Delta t}{1 + z} \quad (3.1)$$

where  $R$  is the radius of the emitting region,  $\delta$  is the Doppler factor (the ratio of the observed to intrinsic frequency),  $\Delta t$  is the observed variability timescale,  $z$  is the redshift of the galaxy, and  $c$  is the speed of light [29].

### 3.6.2 Relativistic Jets

As previously stated, blazars are a class of AGNs that have a collimated jet of relativistic particles oriented in the direction ( $\sim 0^\circ$ ) of the observer's line of sight. These jets originate in highly energetic processes in the universe, are of a non-homogeneous nature, and have parsec scales. Blazar observations are important for understanding the mechanisms that originate these jets, as well as their formation, acceleration, and collimation [29].

X-ray observations of blazars conducted by [30] established strong constraints on the composition of particle jets [29]. From this study, it was determined that the use of a jet model composed purely of electron-positron pairs results in an overestimation of soft X-ray emission [30]. Whereas the use of a jet model composed purely of proton-electron pairs results in an underestimation of X-ray emission [30].



### CHAPTER 3. ACTIVE GALACTIC NUCLEI (AGN)

In this context, a new widely accepted model was proposed that contemplates two particle flows [31]. It consists of an "inner spine" or relativistic internal flow of electron-positron pairs, which originate in the innermost region of the accretion disk, surrounded by a less relativistic plasma of proton-electron pairs, coming from the entire accretion disk [29].



# Chapter 4

## Particle Interactions

In this chapter, we will address the interactions between particles emitted by galactic or extragalactic sources with the Earth's atmosphere, leading to the production of Atmospheric Air Showers, which will be one of the main points to discuss. Additionally, we will explore the interactions between high-energy charged particles and dielectric media, which result in radiation phenomenon known as the Cherenkov Effect.

### 4.1 Atmospheric Air Showers

The atmospheric air showers were discovered about 85 years ago by physicist Pierre Auger, who observed "coincidences" when placing two or three counters (detectors) in the open air. These coincidences decreased as the separation between the counters increased, thus suggesting the existence of a phenomenon that he termed air shower [32]. These are cascades initiated by primary particles coming from outside the planet when they interact with the Earth's atmosphere. An air shower has an electromagnetic, a muonic, a hadronic, and a neutrino component [33]. As such, air showers are used to detect particles with very high energies, which are difficult to measure with satellites outside the atmosphere (whose collection area is very limited) since the particle flux follows a power law. This means that the higher the energy, the lower the expected particle flux [34].

From the detection of the secondary particles of the air shower that impact the surface of the detectors, algorithms are used to reconstruct the direction, energy, and type of primary particle that collided in the Earth's atmosphere, solving the problem of the poor flux of high-energy particles [34]. Therefore, an air shower can be generated by any particle entering the Earth's

## CHAPTER 4. PARTICLE INTERACTIONS

atmosphere. However, we will focus on showers generated by two types of particles: gamma rays (what we wish to measure) and hadrons (main background).

### 4.1.1 Gamma rays as primary particles

The air showers generated by gamma rays primarily consist of electromagnetic components. The interactions involved in the production of secondary particles occur through pair production, Bremsstrahlung and Coulomb scattering. The air shower propagates in this way, forming a front of particles, whose lateral distribution can be obtained by primarily considering, among other interactions, the effect of Coulomb scattering, which determines the characteristic size of the front [3]. Next, the first two previously mentioned interactions will be detailed.

Regarding pair production, it involves the interaction between a high-energy gamma ray (above 1 MeV) and an atmospheric nuclei, resulting in a pair particle and antiparticle, in this case, an electron (particle) and a positron (antiparticle). Thus, pair production provides matter and antimatter. For pair production to occur, it is necessary for the incident gamma ray to have, at a minimum, the rest energy of both produced particles, that is,  $E_{\min} = 2m_e c^2 \sim 1.02 \text{ MeV}$  [29]. Bremsstrahlung (braking radiation) consists of the deceleration of charged particles and the emission of a 'Bremsstrahlung' photon as a result of scattering in a Coulomb field [33], where the energy ( $E_p$ ) of the particle is much greater than its rest energy ( $E_0 = m_p c^2 \ll E_p$ ). In this way, the high-energy particle, compared to  $E_0$ , decelerates over a very short distance due to the presence of a Coulomb field, emitting radiation [29].

A simple model introduced by Heitler [35] discusses the basic structure for purely electromagnetic air showers, but it can be applied to air showers with a hadronic primary particle. Heitler's model considers branching in air showers, as can be seen in Fig. 4.1. Each line can be interpreted as a particle (or energy packet) that eventually divides, at each vertex, where similarly, energy splits into two. Each branching occurs after a collision length ( $\lambda$ ), so after  $n$  branchings, there will be  $N(X) = \frac{2X}{\lambda}$  segments, where  $X$  is the slant depth along the shower [3].

The energy of each particle will decrease as the depth  $X$  increases, in such a way that  $E_p(X) = \frac{E_0}{N(X)}$ . However, it will not reach zero because there is a "critical" energy ( $E_c$ ) for the splitting processes, beyond which the particles only lose energy, get absorbed, or decay. The critical

## CHAPTER 4. PARTICLE INTERACTIONS

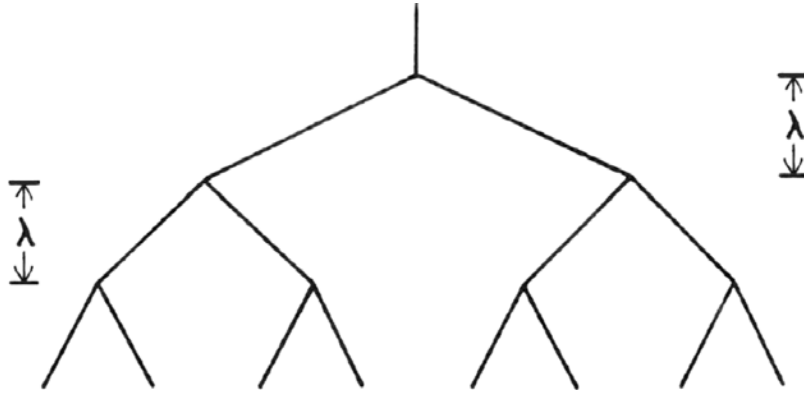


**Figure 4.1:** Diagram of the lateral distribution of particle production in the Heitler model for electromagnetic air showers [3].

energy value for air showers is approximately  $E_c \approx 87 \text{ MeV}$  [3]. From the above, the number of particles at the maximum of the air shower in this model can be calculated as

$$N(X_{\max}) = \frac{E_0}{E_c} \quad (4.1)$$

and similarly, the maximum depth of the shower as

$$X_{\max} = \frac{\lambda \ln \left( \frac{E_0}{E_c} \right)}{\ln 2}. \quad (4.2)$$

The remarkable feature of this model is that the equations 4.1 4.2 are valid for electromagnetic air showers and, in an approximation, for hadronic showers, which means that

$$N_{\max} \propto E_0 \quad \& \quad X_{\max} \propto \ln(E_0). \quad (4.3)$$

Thus, an approximation can be given to the physics behind gamma-ray-initiated air showers: when a gamma ray with energy greater than 1.02 MeV (greater than the rest energy of the electron-positron pair) enters the Earth's atmosphere and interacts with an atmospheric nucleus, it can produce an electron-positron pair. These pairs interact through Coulomb scattering with atmospheric nuclei and continue to propagate in the atmosphere until, eventually, each emits a secondary gamma ray through Bremsstrahlung within a radiation length, which has lower energy than the primary gamma ray. In this way, these lower-energy secondary gamma rays will produce more electron-positron pairs, which will produce more gamma rays, causing the process to continue, exponentially increasing the number of particles and exponentially decreasing the average energy of the particles, until one of the particles reaches the critical energy

$E_c \approx 87$  MeV where particle production begins to cease, a point known as the maximum of the air shower[29].

### 4.1.2 Hadrons as primary particles

Air showers generated by hadronic particles or atomic nuclei (in general, cosmic rays) occur with a much higher probability than air showers initiated by gamma rays, due to the greater flux of cosmic rays in comparison (over 99.9%). They hadronic air showers consist of electromagnetic, muonic, and hadronic components. The production of secondary particles (e.g., muons, photons, and others) is primarily based on the decays of charged kaons and pions, as well as neutral pions. Some of the decay channels and their branching ratios are as follows:

$$\begin{aligned}
 \pi^\pm &\rightarrow \mu^\pm + \nu_\mu (\bar{\nu}_\mu) & (\sim 100\%) \\
 \pi^0 &\rightarrow \gamma + \gamma & (\sim 98.8\%) \\
 K^\pm &\rightarrow \mu^\pm + \nu_\mu (\bar{\nu}_\mu) & (\sim 63.5\%)
 \end{aligned} \tag{4.4}$$

Hadronic cascades predominantly produce pions and have only a 10% probability of producing kaons. When neutral pions decay (see second equation in 4.4), they give rise to photons that initiate electromagnetic cascades with electron-positron pair production (see Fig. 4.2:  $\gamma, e$  component), which are considered the "soft" component due to their relatively easy absorption. Charged pions and kaons may either interact or decay, and the competition between decay and interaction probabilities depends on the energy. For the same Lorentz factor, kaons ( $\tau = 12.4ns$ ) have a higher decay probability than pions ( $\tau = 26ns$ ). Their semileptonic decays are illustrated in first and third Equations 4.4, demonstrating the production of muons and neutrinos (see Fig. 4.2:  $\mu, \nu$  and hadron components). Muons can undergo decay processes through the channels  $\mu^+ \rightarrow e^+ + \nu_e + \bar{\nu}_\mu$  or  $\mu^- \rightarrow e^- + \bar{\nu}_e + \nu_\mu$ , contributing to the electromagnetic component via electrons/positrons. Muons that do not decay make up the majority of secondary particles at sea level, with an 80% contribution. It is important to note the presence of a neutrino component resulting from the aforementioned decay processes [33].

It can be highlighted that hadronic cascades contain processes considerably different from gamma-ray-initiated air showers. Finally, it is worth mentioning that there is also a "splitting model" developed by Heitler-Matthews to describe the physics of hadronic air showers, which

## CHAPTER 4. PARTICLE INTERACTIONS

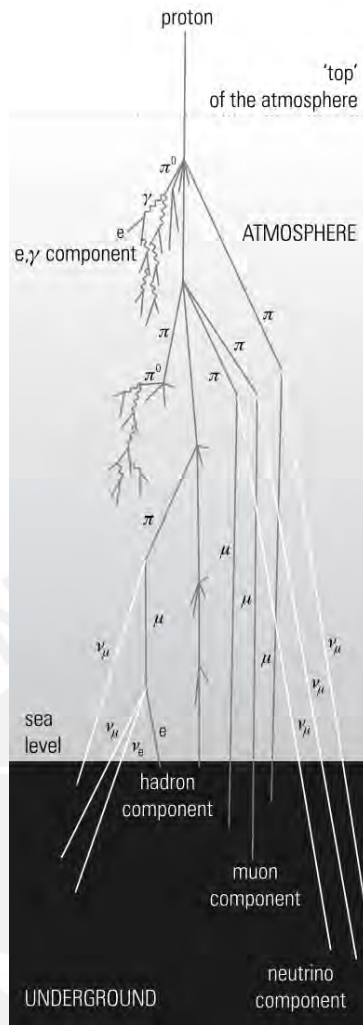


**Figure 4.2:** Lateral view of the production of secondary particles in an air shower with a proton (hadron) as the primary particle, showing the electromagnetic, muonic, and hadronic (pions) components [33].

will not be covered in this thesis [3].

### 4.2 Cherenkov Effect

Since its discovery in 1934 by the Soviet physicist Pavel Cherenkov, the Cherenkov effect has played a fundamental role in the detection of high-energy particles. This optical phenomenon occurs when a charged particle (with charge  $z$ ), moving in a dielectric medium with a refractive index ( $n$ ), travels at a velocity ( $v$ ) greater than the speed of light in that medium ( $c_n = c/n$ ), emitting electromagnetic radiation (Cherenkov) spanning the blue optical spectrum [33]. When particles enter a dielectric medium at this velocity, they generate a conical front of waves, which can define the direction of Cherenkov radiation (see Fig. 4.3). This Cherenkov effect results in a loss of the particle's energy, so it can only occur when:

## CHAPTER 4. PARTICLE INTERACTIONS

$$v \geq \frac{c}{n} \text{ or, equivalently, } \beta = \frac{v}{c} \geq \frac{1}{n}. \quad (4.5)$$

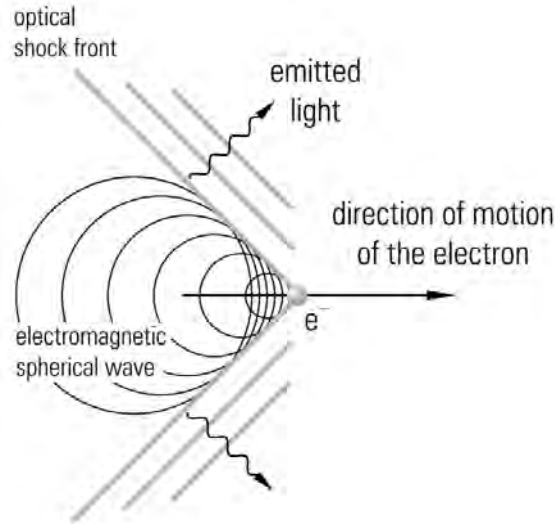


**Figure 4.3:** Cherenkov effect produced by particles passing through a dielectric medium with a refractive index  $n$  at a velocity exceeding the speed of light in that medium ( $v > c/n$ ) [33].

There is also an angular restriction, or Cherenkov angle, related to the direction of the particle's velocity  $v$  [33], given by:

$$\theta_C = \arccos \frac{1}{n\beta} \quad (4.6)$$

Due to this effect, a certain number ( $N$ ) of Cherenkov photons are emitted isotropically in the visible spectrum ( $\lambda_1$ : 400 -  $\lambda_2$ : 700 nm) [33], which can be calculated as:

$$\begin{aligned} \frac{dN}{dx} &= 2\pi\alpha z^2 \frac{\lambda_2 - \lambda_1}{\lambda_1 \lambda_2} \sin^2 \theta_C \\ &\approx 490z^2 \sin^2 \theta_C \text{ cm}^{-1}. \end{aligned} \quad (4.7)$$

The equations presented strongly depend on the refractive index of the medium ( $n$ ). Therefore, the physics behind these effects must be formulated taking into account this parameter. Below, we will detail two media, air and water, with particular emphasis on the latter, as the proposed detector, which will be discussed later, relies on the Cherenkov effect in water.

### 4.2.1 Air Cherenkov effect

The refractive index in air is  $n = 1.000273$  (at 20°C and 1 atm), which can be used to determine, using Eq. 4.6, that the Cherenkov angle for relativistic particles in air is  $\approx 1^\circ$ . Furthermore,

## CHAPTER 4. PARTICLE INTERACTIONS

using Eq. 4.7, it is determined that for a relativistic particle with charge ( $z = 1$ ), 30 Cherenkov photons are produced per meter [33].

The observation of air showers initiated by gamma rays, exploiting the Cherenkov effect in air, involves the use of Cherenkov telescopes (based on the technique of Cherenkov air imaging) that detect the traces of this radiation generated by charged particles in the shower, on the ground, known as the Cherenkov light pool. Therefore, a telescope located at some point within this "pool" can detect air showers if its mirror area is large enough to collect sufficient Cherenkov photons. However, with a single telescope, it is challenging to reconstruct the exact geometry of the air shower. Thus, strategically separated multiple telescopes (telescope array) are necessary to observe the cascade from different points and enable stereoscopic reconstruction of the shower [36].

Some of the most relevant gamma ray observatories based on Cherenkov telescopes as of the publication date of this thesis are:

- **HESS (High Energy Stereoscopic System) Telescopes.** Since 2002 - Namibia [37].
- **VERITAS (Very Energetic Radiation Imaging Telescope Array System).** Since 2007 - Arizona [38].
- **MAGIC (Major Atmospheric Gamma Imaging Cherenkov Telescopes) Telescopes.** Since 2004 - La Palma, Canary Islands, Spain [39].
- **CTA (Cherenkov Telescope Array).** Under development - Two locations: Atacama (Chile: SOUTH) & La Palma, Canary Islands (Spain: NORTH) [40].

Observatories based on Cherenkov telescopes have achieved excellent results and have discovered numerous astrophysical sources due to their high angular resolution, the focusing and imaging techniques used, and the fact that they detect gamma rays at low atmospheric depths (soon after their development in the atmosphere). However, these facilities come with limitations such as their observation energy range, limited field of view ( $3^{\circ}$ - $8^{\circ}$ ), dependence on atmospheric conditions and nighttime operation. For these last two reasons, it is unlikely that such observatories will detect transient and variable events. This has paved the way for the con-



## CHAPTER 4. PARTICLE INTERACTIONS

struction of other types of gamma-ray observatories, such as those based on Cherenkov water tanks [41].

### 4.2.2 Water Cherenkov effect

The refractive index in ultra-pure water is  $n = 1.3333$  (at 20°C and 1 atm), which can be used to determine the minimum energy required for a particle to produce this effect, which depends on the mass of the particle ( $E_{\text{min}\mu\text{on}} = 160.32$  MeV and  $E_{\text{min}\text{electron}} = 0.775$  MeV). Using Equation 4.6, it can be determined that the Cherenkov angle for relativistic particles in air is  $\approx 41.4^\circ$ . Furthermore, using Equation 4.7, it is determined that for a relativistic particle with charge ( $z = 1$ ), 220 Cherenkov photons are produced per centimeter [33].

Given the operational limitations previously described in Cherenkov telescopes, the concept of constructing detector arrays at high-altitude sites was conceived. This setup would allow for the early detection of air showers before they reach their maximum depth and the particle production begins to cease, as well as being sensitive to transient and highly variable events.

Currently, a method without such limitations, yielding excellent results, is based on arrays of water Cherenkov tanks. Such an array consists of a large number of tanks filled with water with photomultipliers (PMTs or PETs) located inside. Particles from atmospheric showers reach the surface of the tanks, and as they pass through the water, they generate Cherenkov light because they travel faster than the speed of light in water (approximately  $0.77c$ ) [41].

Some of the most relevant gamma ray observatories based on Cherenkov Tanks Array as of the publication date of this thesis are:

- **HAWC (High-Altitude Water Cherenkov Observatory) - 4100** . Since 2015 - Sierra Negra, Mexico - 4100 masl [42]
- **LHAASO (Large High Altitude Air Shower Observatory)**. Since 2021 - Sichuan, China - 4410 masl [43]
- **SWG0 (The Southern Wide-field Gamma-ray Observatory)**. Under development - South America [44]

## Chapter 5

# The Southern Wide-field Gamma-ray Observatory (SWGGO)

Observatories based on arrays of Cherenkov water tanks on the surface have revealed significant scientific potential for studying the cosmos, such as the localization of galactic and extragalactic sources. Current instruments like HAWC have confirmed this potential with multiple results obtained from their operations. These results are being complemented in the Northern hemisphere by the LHAASO observatory [43] in China. However, there is no such observatory in the Southern hemisphere, leaving a gap in sky access for transient and variable phenomena. Based on these premises, the project 'The Southern Wide-field Gamma-ray Observatory (SWGGO)' is born. It will be an astrophysical observatory based on the Cherenkov effect in water and will be located at high altitude in South America, over 4.4 km above sea level. It will consist of more than 6,000 unit detectors deployed in a specific array and can extend over a surface or be submerged in a lake. Currently, both the type of detector units (tanks) and the configuration of the tank array are not yet fixed. In this chapter, a specific type of tank (A1) and the reference configuration [45] used for R&D studies will be used, a configuration that would be covering just under 0.30 km<sup>2</sup> with detector units containing several thousand tons of water. The motivations for SWGGO include access to the galactic center and the complementarity with the gamma-ray experiment CTA-South, as well as the study of cosmic rays [44].

### 5.1 Specifications

Some specifications, that can be found on the collaboration's white paper [44], include:

## CHAPTER 5. THE SOUTHERN WIDE-FIELD GAMMA-RAY OBSERVATORY (SWGGO)

- Based on ground-level particle detection using water Cherenkov detector units.
- Wide field of view : To measure TeV halos, the morphology of the Galactic Center, study the nature of the Fermi Bubbles, among others.
- Duty cycle close to 100% : Due to the Cherenkov water tanks will detect virtually at any moment of their operation the entire range they are covering, this aids in the observation of transient events.
- Instantaneous field of view in order steradian: Due to the three-dimensional area that will be observed and the observational aperture that the tanks will have.
- Latitude between 10° and 30°S in South America: To observe areas of the Milky Way not accessible from the Northern Hemisphere due to its geographical location, lacking a gamma-ray observatory based on Cherenkov water tanks.
- Altitude of 4.4 km or higher: To detect the particles from the air shower as close as possible to the starting point (the first interaction between the primary particle and the atmosphere  $\gtrsim 15 - 35\text{Km}$  above sea level).
- Energy ranges from 100s of GeV up to the PeV scale: For the detection of sources emitting at such energies as well as the search for dark matter annihilation/decay.
- High fill-factor core detector: An area larger than HAWC and better sensitivity

Say that the different types of tanks are being evaluated for the final array, and that A1 was chosen because it was adopted as the reference configuration for the R&D studies.

Different types of tanks evaluated by the SWGGO collaboration for the final array and the tank to be used in this thesis (type A) can be seen in Fig. 5.1. There, tanks with circular cross sections of different diameters, heights (of the tank and the water filling level), and different PMT configurations (single and dual layer: 2 PMTs in a single unit, with opposite observation directions) are shown (for example, tanks of types A, B, C, D, and F have a central PMT, while tank type E has a configuration of 3 peripheral PMTs) [46]. The detailed specifications of the A1 tank, which will be used in this thesis, are as follows:

## CHAPTER 5. THE SOUTHERN WIDE-FIELD GAMMA-RAY OBSERVATORY (SWG0)

- **Tank Diameter:** 3.82 m
- **Total Height:** 3.00 m
- **PMT Configuration:** 1 PMT in each of the two layers located in the center of the tank at the height of the separation level between the two chambers, pointing upwards and downwards, respectively.
- **Filling Level and Division Height:** 0.50 m (the central PMT will be placed at the center of this division)

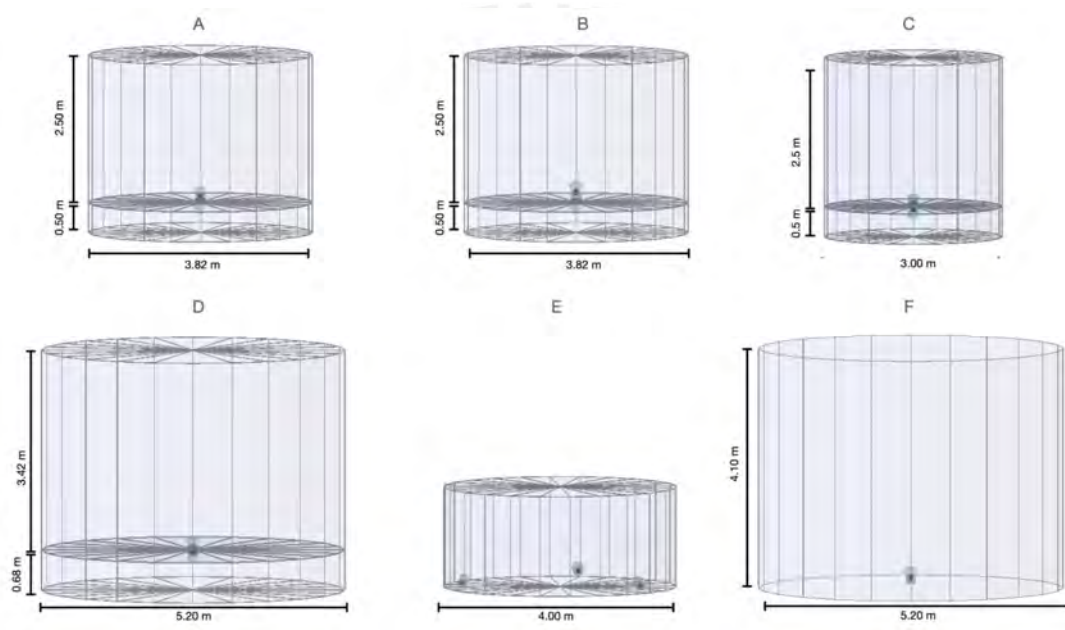


**Figure 5.1:** Different types of tanks (unit designs) evaluated by the SWGO collaboration for the final array. Each of these has different radii, heights, and PMT configurations [46].

The PMTs used in the type A tank will be located in the central part of a division within the tank at the height of the separation level between the two chambers, pointing upwards and downwards, respectively. That is, they will point towards the upper lid of the tank (upwards) and towards the base (downwards). The internal report proposes the purchase of PMTs from Hamamatsu (for example, PMT: 8" = Hamamatsu R5912).

In addition to the proposals mentioned, it is worth noting that the Peruvian site candidates (which will be detailed later) open the possibility of placing detectors inside lakes or artificial ponds. The reference configuration for SWGO (see Fig. 5.2) to be used consists of an array of tanks with two cores of different tank concentrations: an inner core with high density using a hexag-

## CHAPTER 5. THE SOUTHERN WIDE-FIELD GAMMA-RAY OBSERVATORY (SWG0)

onal grid of tanks with a grid spacing of 4.03 m for a high probability of detecting secondary particles produced in air showers, and an outer core with a lower density of identical tank units to those in the central array, serving as a support array that effectively provides high energy sensitivity for the detection of peripheral particles. Detailed specifications can be found in [45].

Some important characteristics are:

- **Internal core:** 160 m radius circle =  $80,400m^2$  with  $\approx 80\%$  fill factor (exactly 80.7%) of the area covered by 5,719 Cherenkov detector units.
- **External core:** 300 m outer radius =  $202,200m^2$  with  $\approx 5\%$  fill factor of the area covered by 880 Cherenkov detector units.

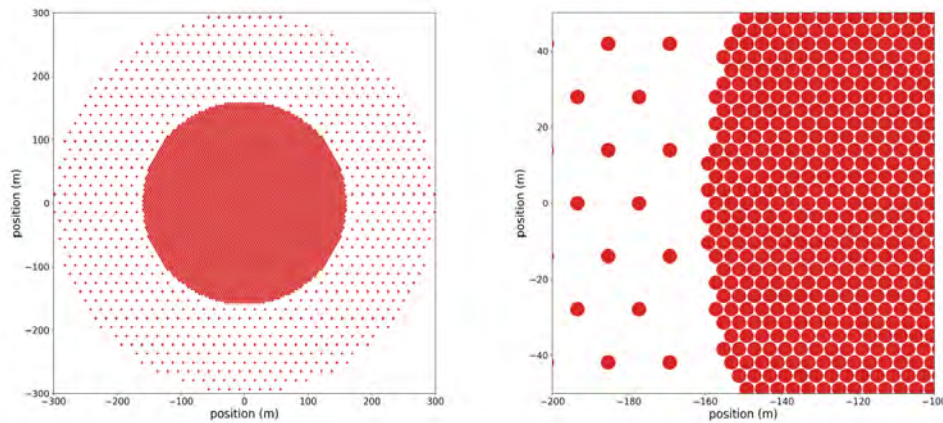


**Figure 5.2:** Left: Internal and external configuration (core) of the tank array. Right: Close-up of the boundary between the internal and external core. [45].

### 5.2 Science Case

The science case of SWGO encompasses a wide range of topics, including the study of galactic sources to extragalactic sources. An area of particular interest for SWGO is the investigation of Fermi bubbles (see Fig.5.3) emanating from the center of our galaxy (of high importance to SWGO due to its southern latitudes), as well as the observation and discovery of PeVatrons sources, cosmic ray observations, and supernova remnants, in addition to regions of stellar formation and diffuse galactic emission [47].

SWG0 will be configured as a Cherenkov water tank-based observatory with a broad field of view, providing it with the necessary sensitivity to investigate transient events. Among these

## CHAPTER 5. THE SOUTHERN WIDE-FIELD GAMMA-RAY OBSERVATORY (SWGGO)

events, research related to active galactic nuclei stands out, including the search for new VHE Blazars, the study of high-frequency extreme BL Lacs, the development of AGN emission models, the investigation of the variability and periodicity of blazars, among other aspects.

In addition to the mentioned transient events, SWGGO will also focus on the detection of gamma-ray bursts and gravitational waves. Furthermore, observations will be conducted at multiple wavelengths, and various cosmic messengers will be explored, including, of course, the search for new transient phenomena.

Finally, SWGGO will also address issues related to physics beyond the Standard Model, such as the search for dark matter candidates, the study of primordial black holes, and tests of Lorentz invariance, among other high-interest science cases.

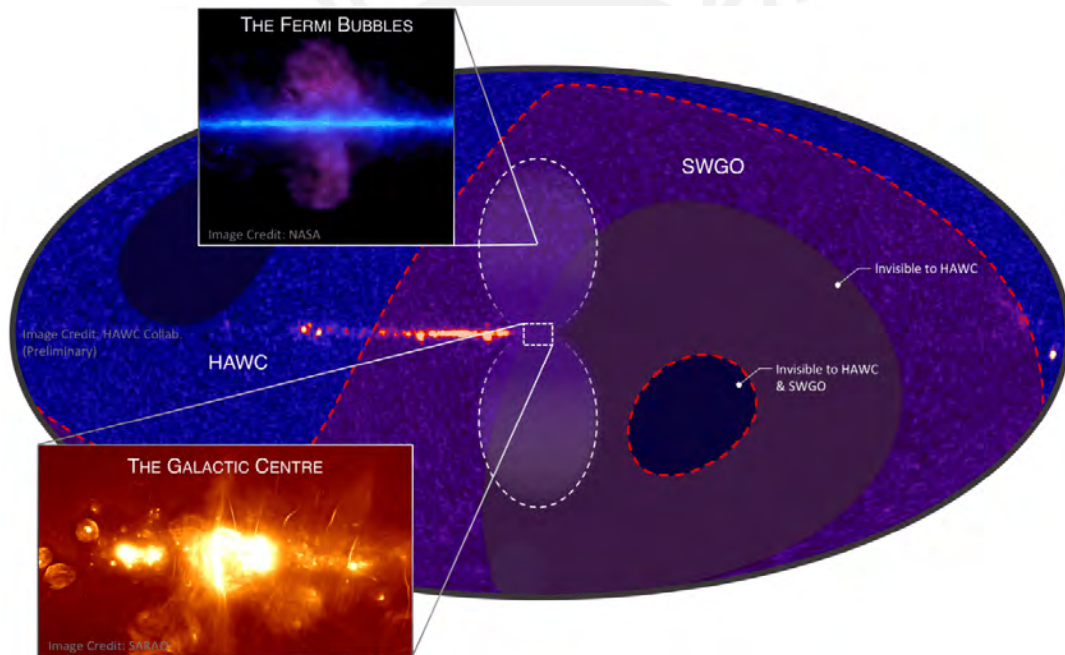


**Figure 5.3:** The SWGGO observation zone (bounded by the red dashed lines) encompasses the galactic center (at the center of the image) and the Fermi bubbles (bounded by the white lobular-shaped lines perpendicular to the galactic plane) [47].

### 5.2.1 Blazars observable in the Southern hemisphere (by SWGGO)

Among the extragalactic sources that will be observable by SWGGO, blazars are chosen to be further explored in this thesis. As an example, a selection of fourteen blazars observable from Southern latitudes is presented below. This selection has been made taking into account their location in the SWGGO field of view. The choice is based on the FERMI 4FGL-DR4 catalog [48]



## CHAPTER 5. THE SOUTHERN WIDE-FIELD GAMMA-RAY OBSERVATORY (SWGGO)

that covers energies from 50 MeV to 1 TeV, serving as representative examples of what SWGGO could be capable of observing at energies from hundreds of GeV to the order of PeV. This approach provides a view of the wide observable area of SWGGO and the types of astronomical objects that will be within its reach.

In Fig.5.4, with gradient colors (each color represents a  $10^\circ$  latitude ring), the regions accessible to SWGGO are shown. The central black ellipse, which is an area non-observable by SWGGO, is noteworthy because one would need to be located at the South Pole to access it. In general, the black zones will not be considered for searching observable blazars.

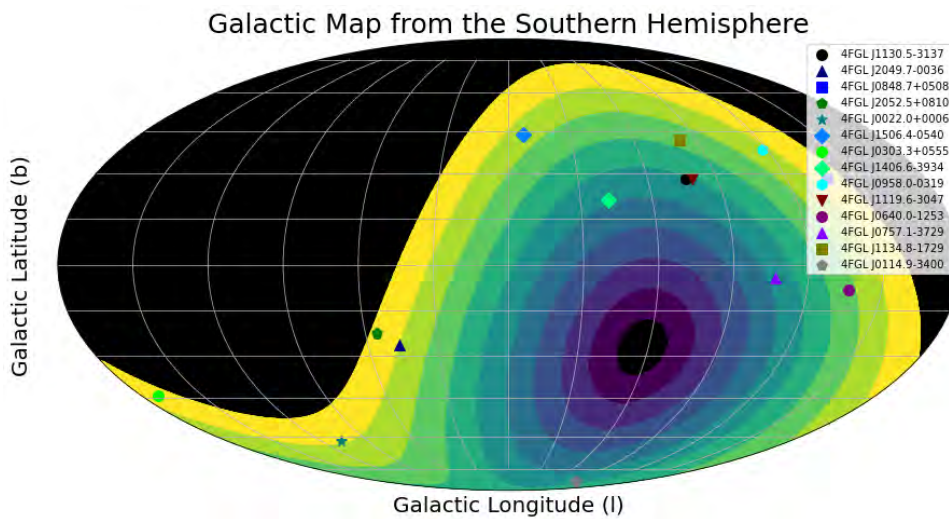


**Figure 5.4:** Representation of fourteen blazars extracted from the FERMI 4FGL-DR4 catalog [48] located in southern latitudes, observable zones by the future SWGGO. Each color represents a ring with  $10^\circ$  of latitude and the black zones represent unobservable latitudes (and not analyzed).

In total, the fourteen sources represented in 5.4 are located away from the central horizontal line where the galactic plane is located, as expected, given that the luminosity of galactic sources, mostly, overshadows the luminosity of more distant sources (e.g. extragalactic sources like blazars). The energy cut used is for pivot energy greater than 10 GeV.

The specifications such as the coordinates and Pivot Energy can be seen in Table 5.1.

## CHAPTER 5. THE SOUTHERN WIDE-FIELD GAMMA-RAY OBSERVATORY (SWG0)

**Table 5.1:** Blazars candidates that could be observable by SWGO. The data were extracted from the LAT 12-year Source Catalog (4FGL-DR4) [48]. Pivot Energy is the energy (in MeV) with the smallest error in differential photon flux derived from the Likelihood analysis for energies between 100 MeV - 1 TeV.

| Name (LAT Catalog) | Galactic Longitude | Galactic Latitude   | Pivot Energy     | Class |
|--------------------|--------------------|---------------------|------------------|-------|
| 4FGL J1130.5-3137  | 283.4387512207031  | +28.1716251373291   | 24721.787109375  | bll   |
| 4FGL J2049.7-0036  | 46.85406494140625  | -26.378036499023438 | 22467.9453125    | bll   |
| 4FGL J0848.7+0508  | 222.26087951660156 | +28.355443954467773 | 19270.6484375    | bll   |
| 4FGL J2052.5+0810  | 55.42718505859375  | -22.283302307128906 | 18832.607421875  | bll   |
| 4FGL J0022.0+0006  | 107.20703887939453 | -61.85816955566406  | 18064.90625      | bll   |
| 4FGL J1506.4-0540  | 352.855712890625   | +43.72444534301758  | 14091.6953125    | bll   |
| 4FGL J0303.3+0555  | 171.83876037597656 | -44.06387710571289  | 13787.6083984375 | bll   |
| 4FGL J1406.6-3934  | 318.3714904785156  | +21.03311538696289  | 13123.037109375  | bll   |
| 4FGL J0958.0-0319  | 242.11038208007812 | +38.289894104003906 | 12405.5205078125 | bll   |
| 4FGL J1119.6-3047  | 280.6370544433594  | +28.07337760925293  | 11621.025390625  | bll   |
| 4FGL J0640.0-1253  | 223.2143096923828  | -8.321293830871582  | 11216.5966796875 | bll   |
| 4FGL J0757.1-3729  | 253.17176818847656 | -4.468254089355469  | 10712.009765625  | bll   |
| 4FGL J1134.8-1729  | 278.17974853515625 | +41.663543701171875 | 10521.525390625  | bll   |
| 4FGL J0114.9-3400  | 268.03240966796875 | -81.46336364746094  | 10327.9638671875 | bll   |

### 5.3 Site Candidates

SWG0 will be a gamma-ray observatory at an altitude of at least 4.4 km above sea level, located in the Southern hemisphere at a latitude between 10 and 30 degrees south. Some locations with these characteristics are found in the Andes mountain range (i.e. South America). The following is a brief review of the evaluation of high-Andean sites as candidates for hosting SWGO. Details such as altitude, proximity to a lake, electrical availability, among others, will be described in the following lines.



## CHAPTER 5. THE SOUTHERN WIDE-FIELD GAMMA-RAY OBSERVATORY (SWGGO)

### 5.3.1 Peruvian candidates

In Peru, three of the locations proposed by SWGO for the construction of the future observatory are located. Peru is the only country, among the candidates, that could host either of the two types of arrays: Ground Array (Imata or Yanque) and Lake Array (Sibinacocha). Each of these will be detailed below.

#### Imata site

Imata is a locality in Arequipa-Peru situated at approximately 4500 meters above sea level at a latitude of 15.8°S. There is a large and flat area where detector units could be located, in total, there is an area of 5.64 km<sup>2</sup> available (see Fig. 5.5), sufficient for the observatory which requires 1 km<sup>2</sup>. In addition, there are two nearby lakes (Jayuchaca Lake and San Antonio de Chuca Lake) and a river with clear water (running along the lower corner of the land, see Fig.5.5) that can be used as a water source. The temperature is around 12°C during the day and at night it drops to -2°C in summer and -10°C in winter. Regarding precipitation, the rainy season runs from December to March, and snowfall is scarce and rare, so there are no issues with snow blockages [49].



**Figure 5.5:** Total area available at the Imata-Arequipa location, with the boundary of the available area outlined in yellow [49].

Finally, it is worth mentioning that this thesis will be focused on simulations conducted at this

## CHAPTER 5. THE SOUTHERN WIDE-FIELD GAMMA-RAY OBSERVATORY (SWGGO)

location in Arequipa due to its extensive and flat available area.

### **Yanque site**

Yanque is near Arequipa (a Peruvian region that is easily accessible by flights from Lima). Arequipa could serve as HQ to reach the site. There is a flat area with an average slope of 3% with two nearby lakes. Yanque is located at an altitude of 4950 meters and at a latitude of 15.8°S [50].

### **Lake Sibinacocha site**

The Sibinacocha site is located in Cusco, a Peruvian region accessible by flights from Lima. It is situated at an altitude of 4869 meters above sea level and at a latitude of 13.85 °S, and it contains three bodies of water: the Cochachaca, Cochauma, and Sibinaccha lagoons. The average temperature is 3 °C, and throughout the year the temperature remains above zero, while in winter it can drop to around -2 °C. The rainy season occurs from December to February, and access is generally not blocked by rain or snow. Cochauma has an ellipsoidal area of 1.2 x 0.9 Km with a maximum depth of 33.02m, while Cochachaca is similarly sized but irregular in shape with a maximum depth of 30.9m. Sibinacocha is the largest and deepest (57.16m), spanning several kilometers in width and length. This site is proposed for a lake array [51].

### **5.3.2 Other candidates**

1. **ALPACA Site (La Paz - Bolivia):** The ALPACA experiment is a project for the observation of gamma and cosmic rays directed between Bolivia and Japan (recently, Mexico has joined). Located in Bolivia, it is situated on the Chacaltaya Plateau in La Paz-Bolivia at an altitude of 4740 meters above sea level with a latitude of 16°23'S. This site is virtually ruled out due to its limited available area (main area of 0.72 km<sup>2</sup> and additional area of 0.12 km<sup>2</sup>), insufficient to accommodate the 1 km<sup>2</sup> required for SWGO [52].
2. **Parque Astronomico de Atacama Site (Chajnantor - Atacama - Chile):** This site is hosted in the Parque Astronomico de Atacama State concession. Situated at an altitude 4625 m a.s.l. and around 22.9481°S latitude. It is a desert area with favorable atmo-

## CHAPTER 5. THE SOUTHERN WIDE-FIELD GAMMA-RAY OBSERVATORY (SWG0)

spheric conditions for astronomical observation, which is why it hosts various astronomical projects (CCAT, Simons Observatory, and others) [53].

3. **Pampa La Bola (Atacama - Chile):** The site is home to ALMA (Atacama Large Millimeter Array <http://www.almaobservatory.org>), which has a concession for the homonymous project, supported by a collaboration involving NRAO, ESO, NAOJ, among others. It is located at high altitude (4770 m a.s.l.) at a latitude of 22.9447°S [54].
4. **Alto Tocomar (Salta - Argentina):** It is a ground-based proposal with an estimated slope of 1.5% for the inner area of 320m diameter and 2.3% for the 600m diameter area. It is located at an altitude of 4430 m.a.s.l. and a latitude of 24.19°S [55].
5. **Cerro Vecar (Salta - Argentina):** It is a ground-based proposal with a quite irregular flat area, estimated to have slopes of 5-6% for the inner area of 320m in diameter. It is located at an altitude of 4800 m.a.s.l. and a latitude of 24.18°S[56].

### 5.3.3 Assembly Process of a Cherenkov Tank in Peru

Construction of Cherenkov tanks in Peru began through the efforts of Peruvian researchers in collaboration with the University of ADELAIDE and funding from CONCYTEC (Peru). One such tank is currently being built in Lima-Peru, specifically in the Science Faculty at the National University of Engineering (UNI).

The construction and assembly of the tank were supported by members of CONIDA (National Commission for Aerospace Research and Development), UNI, and PUCP (Pontifical Catholic University of Peru) (see Fig.5.6a).

Initially, a considerably flat area was requested in the garden of the UNI Faculty of Science near the electrical connections and a water point for assembly. After importing materials and equipment for the tank assembly at UNI, a trench of 30 cm deep and 3.82 m in diameter was excavated. The acquired tank consists of four outer steel levels that must be assembled one below the other (see Fig. 5.6b).

First, the lower level, consisting of five sections, was assembled using screws and secured with nuts. Once a level is assembled, it is lifted using five hydraulic jacks placed evenly around the

## CHAPTER 5. THE SOUTHERN WIDE-FIELD GAMMA-RAY OBSERVATORY (SWG0)



(a) Cherenkov water tank at UNI lifted by five hydraulic jacks.



(b) Part of the SWGO-Peru team with the newly assembled tank.

**Figure 5.6:** Cherenkov water tank at UNI, Lima-Peru

tank. The lifting is done simultaneously on each jack, requiring at least five people (one per hydraulic jack) to lift the tank. When the tank is suspended with the hydraulic jacks, the next level is placed. This process is repeated until the last level is in place.

A black polyethylene bladder is placed inside the tank, which will be filled with ultrapure water. For this purpose, a filter was installed next to the tank, and with the help of water extraction pumps, the filling process is underway. Currently, the tank is in the process of water filtration and filling.

# Chapter 6

## Simulations using CORSIKA

In this chapter, we will describe the process of simulating air showers with the CORSIKA software. Additionally, we will provide details of the simulation conducted to emulate the tank array configuration proposed by SWGO in [45].

### 6.1 CORSIKA Simulations

CORSIKA is a widely used simulator for air showers initiated by cosmic particles in various astroparticle experiments (HAWC, Pierre Auger, etc.). It recreates, under the Monte Carlo approach, the propagation of particle cascades from the interaction of the primary particle with the atmosphere, emulating subsequent collisions and decays until the absorption of particles reaching critical energy in the atmosphere. CORSIKA takes into account the geomagnetic conditions in which air showers develop (e.g., magnetic field, altitude) and the initial conditions of the primary particle (e.g. type, energy, inclination). CORSIKA uses various models for simulation development, such as VENUS, which studies collisions of heavy ions at ultra-high energies, QGSJET (used to the simulations in this thesis), and DPMJET (dual parton model) [57].

The CORSIKA user guide [57] explains the installation of the code, all necessary input datasets, and the selection of simulation parameters. An example of the input data file can be seen in Fig. 6.1.

Simulations of air showers generated by gamma rays, which will be considered as the signal to be detected, and air showers generated by protons (as the main component of cosmic rays), which will be considered as the noise to be rejected, will be conducted. The simulations were performed using the CORSIKA 7.7500 program with the following specifications at the Imata



## CHAPTER 6. SIMULATIONS USING CORSIKA

|         |                     |   |
|---------|---------------------|---|
| RUNNR   | 1                   | run number  |
| EVTNR   | 1000                | number of first shower event                      |
| NSHOW   | 1000                | number of showers to generate                     |
| PRMPAR  | 1                   | particle type of prim. particle                   |
| ESLOPE  | -2.7                | slope of primary energy spectrum                  |
| ERANGE  | 100000 100000       | energy range of primary particle                  |
| THETAP  | 0. 0.               | range of zenith angle (degree)                    |
| PHIP    | -180. 180.          | range of azimuth angle (degree)                   |
| SEED    | 500 0 0             | seed for hadronic part                            |
| SEED    | 501 0 0             | seed for EGS4 part                                |
| OBSLEV  | 445000              | observation level (in cm)                         |
| QGSJET  | T 0                 | model for high energy hadronic interaction        |
| URQMD   | T 0                 | model for low energy hadronic interaction         |
| QGS SIG | T                   | cross section model for QGSJET                    |
| THIN    | 1.E-2 1.E2 0.       | thinning definition                               |
| THINH   | 10. 10.             | relative threshold and weight for hadron thinning |
| FIXCHI  | 0.                  | starting altitude (g/cm**2)                       |
| MAGNET  | 22.955 -3.849       | magnetic field Imata-Arequipa                     |
| HADFLG  | 0 0 0 0 0 2         | flags hadr.interact.&fragmentation                |
| ECUTS   | 0.3 0.3 0.003 0.003 | energy cuts for particles                         |
| MUADDI  | T                   | additional info for muons                         |
| MUMULT  | T                   | muon multiple scattering angle                    |
| ELMFLG  | T T                 | em. interaction flags (NKG,EGS)                   |
| STEPFC  | 1.0                 | mult. scattering step length fact.                |
| RADNKG  | 200.E2              | outer radius for NKG lat.dens.distr.              |
| LONGI   | T 10. T T           | longit.distr. & step size & fit & out             |

**Figure 6.1:** Example of a CORSIKA input. Each parameter has a comment on the right side detailing the meaning of each variable with its respective units (energy in GeV).

location:

| Energy Range<br>(ERANGE) | Inclination<br>(THETAP)           | Magnetic Field<br>(MAGNET)                         | Observation Level<br>(OBSLEV)    |
|--------------------------|-----------------------------------|--|----------------------------------|
| 100000 – 100000<br>(GeV) | 0. – 0. (°)<br>Vertical Particles | (22.955; 3.849) $\mu$ T<br>Magnetic Field at Imata | 451900 (cm)<br>Altitude at Imata |

**Table 6.1:** Characteristics of the primary particles and the location of the simulations.

The PRMPAR variable refers to the identity of the primary particle. In this case, we will use protons for cosmic or hadronic rays, identified with the number 14, and photons (gamma rays  $\gamma$ ), identified with the number 1.

In the table, the parameter names are presented as headings with their corresponding simulator variable names in parentheses. For the energy range (ERANGE), the same value was used, which indicates a single energy. This is a simplification for this study, the same idea applies to the inclination angle of  $0^\circ$ , interpreted as particles incident vertically on the surface. A more complete study would include larger ranges in these parameters. The magnetic field and altitude are variables that depend on the geomagnetic conditions of the location where the air shower is being simulated (Imata, Arequipa). Such values were extracted from [49].

After the simulation, CORSIKA generates an output file in binary DAT format that needs to be compiled by an internal compiler, which is included when downloading the CORSIKA package,

for the handling of the output data. The units and other details are found in the input headers.

### 6.2 Simulation of the SWGO configuration

The SWGO reference configuration to be used consists of two cores, an inner core with high coverage area and an outer core, with approximately 80.7% and 5% filling, respectively, for the tank configuration (A1) to be used in this thesis.

To conduct the study, one of the detailed geometric configurations in [45] was simulated, using A1 tanks as the detection unit. It comprises a total of 5731 tanks in the inner core with a maximum radius of 160m and 868 tanks in the outer core with radii from 160m to 300m. The simulated configuration can be seen in Fig. 6.2, where the required number of tanks was obtained (5731 internal and 858 external). This arrangement includes a geometric filter that can be used to test whether the secondary particles of an atmospheric shower fall within or outside the array (tank), and a threshold energy filter of 50 MeV [47], which represents the minimum energy a secondary particle falling into the tank must have to be detected. However, real detectors, including their interaction, are not simulated.

As a test example, to determine the number of secondary particles that fall within the array of detector tanks from a single air shower, one of the 100 TeV gamma air shower simulations was used. This simulation generated 6170 secondary particles on the surface. Out of the total number of particles, 81.57% (5033 particles) fell within the detector tanks, while 18.43% fell outside.

#### 6.2.1 Study by Concentric Rings

SWGO is a detector with radial symmetry. Therefore, the proposed study will be conducted using geometric cuts in the detector. Specifically, in the initial stage of the research, cuts of 25m were used. In other words, the tank array is first divided into a circle with a radius of 25m, and then into concentric rings with radii increasing by 25m (the second ring distribution has radii of 25m and 50m, the next one would have radii of 50m and 75m, and so on). Due to the low particle statistics obtained in rings with radii greater than 150m (the outer core of SWGO), it was decided to use rings with a 50m radius to increase particle statistics in each

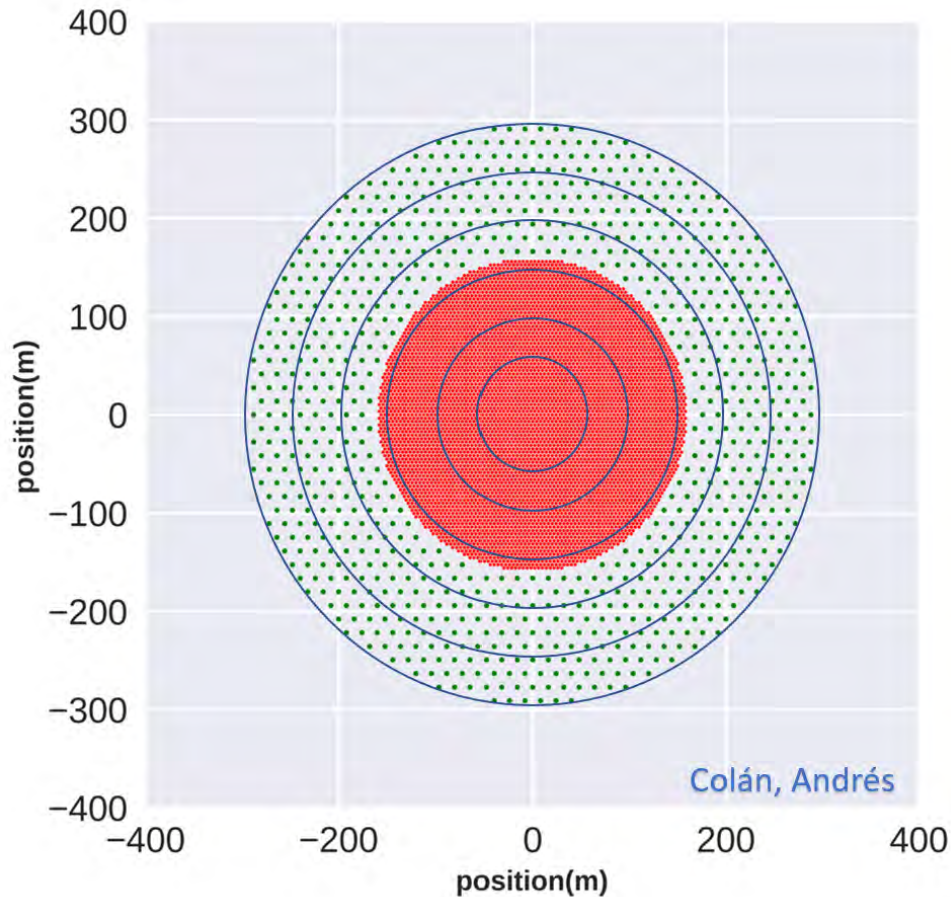


**Figure 6.2:** Simulation of the tank distribution performed by H.E.P. PUCP member Andrés Colán. In red, the tanks that make up the inner core with 80% area coverage can be observed, and in green, the tanks that compose the outer core with 5%. The concentric blue circles have radii that increase by 50 m, dividing the detector array into six sectors to be studied.

sector. The results with the rings increasing their radius by 25m are not presented in this thesis. In other words, the entire area covered by the tanks (maximum radius of 300m) was divided into 6 sectors (rings) of 50 meters radius each, as shown in Fig. 6.2.

Sectioning these regions in a better way will be the subject of study in future research, considering different divisions for the inner and outer core. In addition, the core position could be used as a reference for the array sectioning.



# Chapter 7

## Air Showers Reconstruction

Based on the data provided by the simulations or, in the case of experiments, the data provided by observation, certain algorithms must be applied for the reconstruction. Reconstruction of Air Showers involves the estimation of several parameters, including the core location, direction, and energy. Additionally, specific parameters are required to distinguish between air showers generated by gamma rays (signal) and those generated by cosmic rays or hadrons (noise).

### 7.1 Core Location Reconstruction

The reconstruction of the core of air showers is of high importance for determining the direction and energy of the primary particle that originated it. Air showers propagate along a development axis defined by the incident primary particle. The shower front is denser along this axis (see Fig.7.1) as it is where a large number of its secondary particles are concentrated [58]. From this axis and its intersection with the surface (ground), the core of the air shower is determined, where the maximum energy of the air shower is deposited [59].

Two main methods are employed for this reconstruction: the in-line on-site reconstruction which is performed in real time, and the off-line reconstruction which is carried out after data collection using sophisticated algorithms. Among the strategies to determine the core location are the estimation of the center of mass (COM) of the measured charge and the fitting using specific functional functions, such as the Super Fast Core Fit (SFCF) function [59].

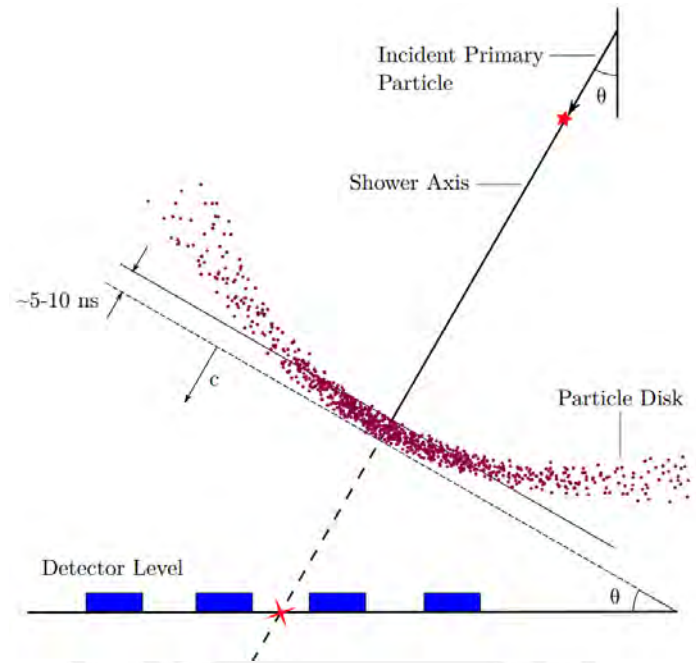


**Figure 7.1:** Air shower front (red dots) with higher particle density near the shower axis defined by the primary particle. Marked with a red star, the reconstructed shower core location from the intersection of the shower axis and the surface [58].

## 7.2 Direction Reconstruction

The process of reconstructing the arrival direction of the particle shower relies on the differences in the timing of impacts recorded by the PMT detectors. As a first approximation, it is considered that the front of the particle shower can be represented as a thin disk (with a nominal thickness of approximately 5 ns) of particles traveling at speeds close to the speed of light. This approximation is valid in the region near the central axis of the shower, where the particles retain the directionality of the primary particle. However, as we move away from the core of the shower, particles undergo multiple scatterings, causing the particle disk to widen and exhibit curvature. To fit this curved front to a plane, it is necessary to take into account the temporal delays due to impacts in the shower tail, requiring a correction of approximately 0.15 nanoseconds per meter from the shower core [58].

Taking these approximations and temporal corrections into account, a  $\chi^2$ -minimization fit is performed, assigning a weight to each PMT based on its measured charge. The resulting values of  $\theta$  and  $\phi$  define the estimated local direction vector of the primary particle [58].

### 7.3 Energy Reconstruction

Energy reconstruction employs algorithms to determine the energy of the primary particle impacting the atmosphere. New algorithms are currently being developed to enhance this reconstruction, and one such algorithm developed at the HAWC observatory will be discussed here: the Template-Based Method for Air Shower Arrays. This method uses templates built from Monte Carlo simulations (CORSIKA) to adjust the observed lateral distribution function (LDF) to an expected probability derived from the simulations. The method's resolution is assessed with simulations, anticipating a strong correlation between the reconstructed and real energy[60].

### 7.4 Gamma-Hadron Separation

From the reconstructions, it is possible to obtain characteristics of the primary particles. However, the reconstructions do not provide information about the identity of the particle. Eventually, there is an interest in studying gamma rays (signal) over cosmic rays (noise) since they do not deviate their trajectory from the source to observation on Earth. Therefore, it is necessary to implement algorithms to differentiate between the two types of air showers.

In various observations made at gamma-ray observatories (e.g. HAWC), it is commonly observed that over 99.9% of the events are generated by cosmic rays of the total detected events [61]. From this, an estimate of the amount of background that SWGO would need to reject can be obtained. Given this enormous difference in the amount of background over the low statistic of signal, it is necessary to implement algorithms to differentiate them. To achieve this, a study is conducted on the differences between both types of cascades, so that, using these variables, it is possible to distinguish between hadronic and gamma-ray air showers. Some of the most common variables include muon count, 68% containment radius, lateral distribution, Compactness, PINCness, LIC, disMax, among others. We will detail some of these below.

Next, the reference variable for gamma-hadron separation that will be used in this research will be developed, as well as some other variables widely used in experiments similar to SWGO (e.g., HAWC, MILAGRO, etc.).

### 7.4.1 Muon Count

One of the previously described differences for air showers initiated by hadrons (cosmic rays) and gamma rays is the difference in the types of particles they produce, such as neutrinos and muons, which initiate the neutrino and muonic components of the cascades [33]. Muons can be relatively easily detected with the Cherenkov water tank method, specifically, with photomultiplier tubes (PMTs) that amplify the Cherenkov signal produced in water.

For the Muon Count study in SWGO, the tank distribution was segmented into the 50 m rings previously described. Then, 1000 hadronic events and 1000 gamma events were simulated at energies from 1 TeV to 100 TeV, in order to count the number of incident muons in each sector. Although it is a small number, it will serve as a baseline study. For each image in Fig.7.2, there are 6 average muon counts (one count per sector), whose error is considered as  $1\sigma$  of the distribution (from the series of a thousand events). This is repeated for energies in steps of 1, 2.5, 5, 7.5, 10, 25, 50, 75, and 100 TeV.

The results are evident; the number of muons present in air showers initiated by hadrons is much greater than in those initiated by gamma rays at all energies (this difference or trend increases with energy). To study and quantify the gamma-hadron separation in each ring, separation in terms of error from Cohen's  $d$  [62] is used, according to the following equation:

$$d = \frac{|Count_{hadron} - Count_{gamma}|}{s} \quad (7.1)$$

with:

$$s = \sqrt{\frac{(n_{hadron} - 1)\sigma_{hadron}^2 + (n_{gamma} - 1)\sigma_{gamma}^2}{n_{hadron} + n_{gamma} - 2}} \quad (7.2)$$

Since  $n_{gamma} = n_{hadron} = 1000$ , Cohen's  $d$  becomes

$$s = \sqrt{\sigma_{hadron}^2 + \sigma_{gamma}^2} \quad (7.3)$$

Separation is quantified by the following equation:

$$d = \frac{|Count_{hadron} - Count_{gamma}|}{\sqrt{\sigma_{hadron}^2 + \sigma_{gamma}^2}} \quad (7.4)$$

## CHAPTER 7. AIR SHOWERS RECONSTRUCTION

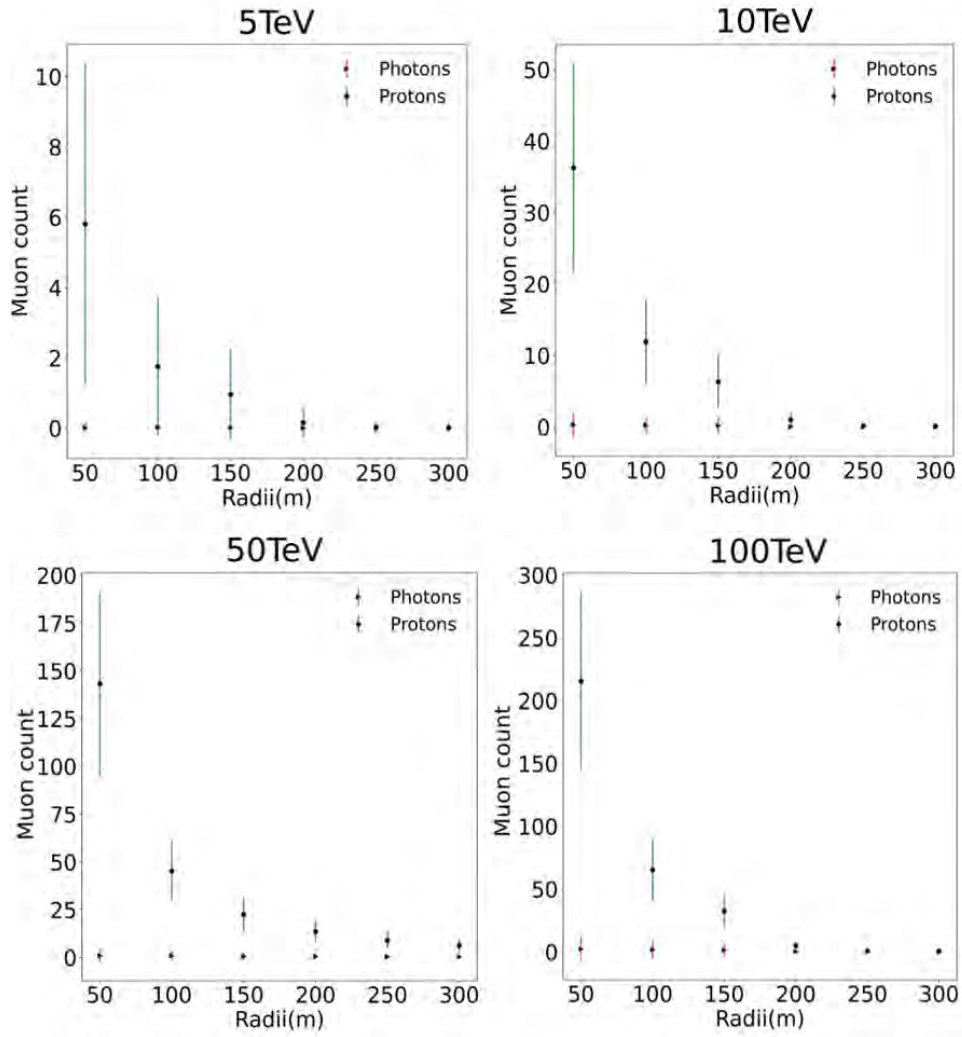


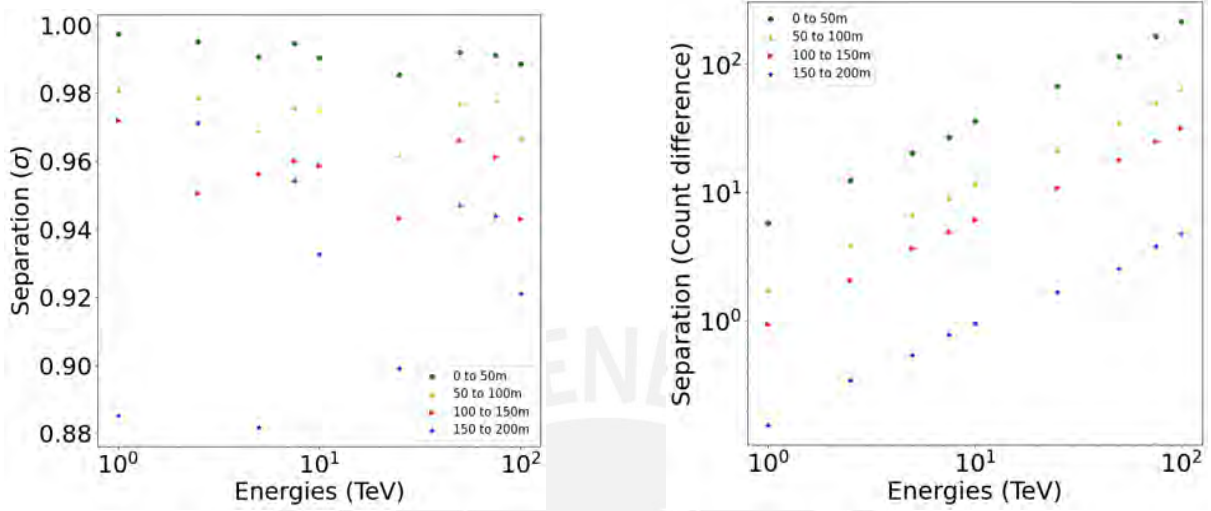
**Figure 7.2:** Muon Counts at different energies (TeV's) using the SWGO tank configuration, considering only the muons that fall within the detector tanks.

The results of using Cohen's  $d$  can be observed in Fig. 7.3a, where the separation for each sector and energy is greater than  $0.88\sigma$ . The sector with the highest separation is from 0 to 50 m with separations greater than  $0.98\sigma$  at all analyzed energies.

Furthermore, in Fig. 7.3b, the average muon count per ring increases with each analyzed energy. Similar to Fig. 7.3a, the sector with the greatest difference, in this case between means of counts, is from 0 to 50 m. These preliminary results are considerably significant and will be detailed later, with the noise rejection and the signal recognition of this variable which are comparable with works carried out in water tank-based observatories, such as HAWC, where they use, for example, machine learning techniques [63] or observables based on the counting of muons and their properties [64].

## CHAPTER 7. AIR SHOWERS RECONSTRUCTION

Furthermore, in Fig.7.3b the average muon count per ring increases with each analyzed energy. Similar to Fig.7.3a, the sector with the greatest difference, in this case between means of counts, is the one from 0 to 50 m.



(a) Gamma-Hadron Separation of muon count in terms of error ( $\sigma$ ) in different rings and energies (1-100TeV)

(b) Separation in terms of the difference between mean muon counts in different rings and energies (1-100TeV)

**Figure 7.3:** Muon Count Gamma-Hadron Separation in SWGO

Given the stability and high gamma-hadron separation in the results for muon count, it was decided to use the number of incident muons on the surface, produced as secondary particles of gamma and hadron air showers in the ring from 0 to 50 m, as the reference variable in this research.

### 7.4.2 Compactness

Compactness is a parameter that uses signals provided by photomultiplier tubes (PMTs) to assess the geometry and distribution of the signal from a detected event [65]. In the context of HAWC Observatory, it is calculated using the following formula:

$$\text{Compactness} = \frac{CxPE40}{nHit} \quad (7.5)$$

where:

- **nHit**: is the number of PMTs activated by the detection of Cherenkov radiation produced by charged particles passing through the water in the detector tank.

## CHAPTER 7. AIR SHOWERS RECONSTRUCTION

- **CxPE40**: is the maximum charge deposited in the photomultiplier tube (PMT) located at a certain distance (d), or more, from the core of the air shower (signal recorded in the PMT farthest from the event's core). In the case of HAWC Observatory, d=40m is used, hence the name "CxPE40".

Compactness assesses the concentration of the signal from the central PMTs compared to that of the farthest activated PMT. A high compactness value indicates that the signal is concentrated in a small area (typical of gamma-ray events), while a low compactness value indicates that the signal is more dispersed (typical of hadronic events) [65].

### 7.4.3 PINCess (Parameter for IdeNtifying Cosmic rays)

PINCness is based on the idea that gamma-ray events exhibit axial symmetry and a smooth, radial lateral charge distribution (LDF) in the detector. In other words, the energy from secondary particles produced by a gamma-ray event is evenly distributed around the event's axis (smooth LDF). In contrast, hadronic events (cosmic rays) tend to have a more irregular (wrinkled) lateral charge distribution due to the presence of heavier particles (e.g. muons) that interact more sparsely [65].

Essentially, PINCness is a  $\chi^2$  (chi-squared) value that quantifies the difference between the effective logarithm of the charge measured in each Photomultiplier Tube (PMT) ( $q_i$ ) and the expected mean value  $\langle q \rangle$  (average of all PMTs within a ring centered on the core of the air shower).

A high PINCness value indicates a smooth LDF (consistent with gamma-ray events), while a low PINCness value suggests a more dispersed LDF (consistent with hadronic events) [66].

### 7.4.4 LIC (Logarithm of Inverse Compactness)

LIC is an empirical parameter developed by the Milagro Collaboration and is calculated as the logarithm of the inverse of Compactness.

$$LIC = \log_{10} \left( \frac{1}{\text{Compactness}} \right)$$

Since it is an increasing function of the inverse of Compactness, the interpretation of this variable is opposite to that of Compactness: high LIC values are typical in hadronic air showers,

## CHAPTER 7. AIR SHOWERS RECONSTRUCTION

while low values are typical in gamma air showers [66].

### 7.4.5 **disMax (Maximum Distance between PMTs)**

disMax is a variable that measures the distance between the two PMTs activated with the most intense signals across the entire detector array in the detected event. Therefore, disMax provides information about how dispersed the signals are in the detector tank array.

Given the typical high dispersion of hadronic events, an event with a high disMax value will be interpreted as hadronic, while events with a low disMax value will be gamma [66].





# Chapter 8

## Air Showers Temporal Distribution

In this chapter, the initial notions of the potential of the temporal distribution as a gamma-hadron separator will be developed. Additionally, several variables generated from the temporal distribution will be provided for analysis.

### 8.1 Analysis of the Temporal Distribution

The fundamental principle for gamma-hadron separation is to find certain differences between hadronic and gamma cascades. Therefore, certain differences between these particle showers will be detailed next, analyzing the temporal distribution of the particles that impact the surface, specifically, those that fall within the detector tanks. Considering that hadronic air showers, due to the production of different types of particles, generate a larger spatial dispersion than gamma air showers. Therefore, it can be inferred that the width of the secondary particle front of the hadronic air shower is narrower but more dispersed.

From CORSIKA simulations, a parameter denoted as  $T(ns)$  is obtained, which represents the time at which the secondary particle impacts the surface. The time starts from the moment the primary particle is injected into the atmosphere (zero time).

To scale the data, a new variable  $Time(ns)$  is added, calculated as the time  $T(ns)$  minus the time  $T(ns)_{min}$  from the distribution of secondary particles for each event. Thus, time begins from when the first particle impacts the surface (zero time). It should be noted that this scaling is done because the distribution (and dispersion) of time, which is indifferent to the initial time, will be used.

From this time, Fig. 8.1 is obtained, where, on the left,  $Time(ns)$  versus the incidence radius

## CHAPTER 8. AIR SHOWERS TEMPORAL DISTRIBUTION

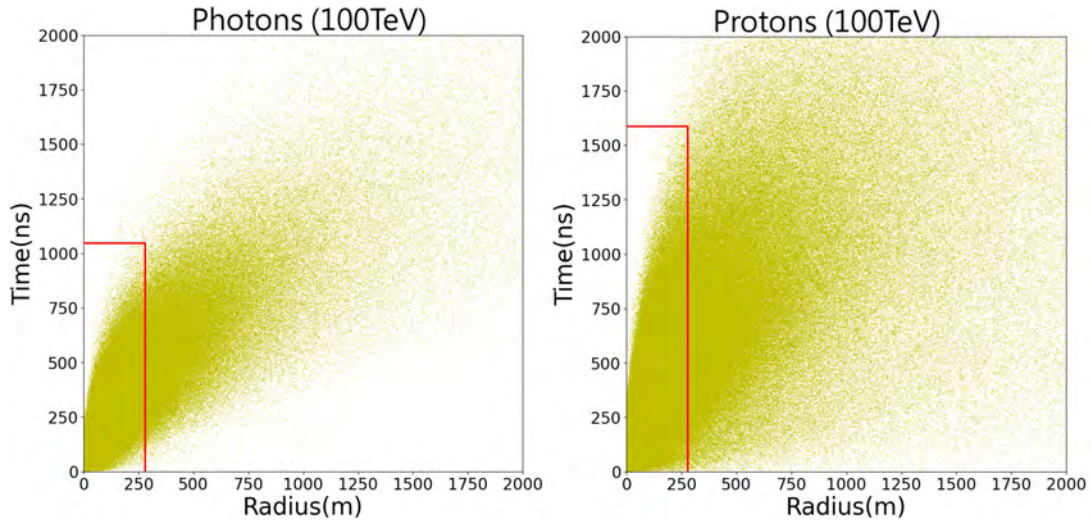


**Figure 8.1:** Distribution of the temporal variable Time(ns) for photons and protons at 100 TeV as primary particles. The red lines indicate the maximum radius that will be used for the study.

of a particle in a gamma event can be seen, while on the right, the same graph for a hadronic event is displayed. The gamma event, as expected, is less dispersed than the hadronic event. This provides a clue that the time of the particle distribution is a candidate for gamma-hadron separation to be analyzed.

An important note is that, since the proposed tank configuration we will use has a maximum radius of 300 m, we will focus only on the temporal distribution at radii, at most, of 300 m (red line in Fig. 8.1). SWGO will be a detector that can cover up to 1 km<sup>2</sup> ( 600 m radius), so it is worth mentioning that for different configuration proposals not covered in this thesis, different cuts would have to be made.

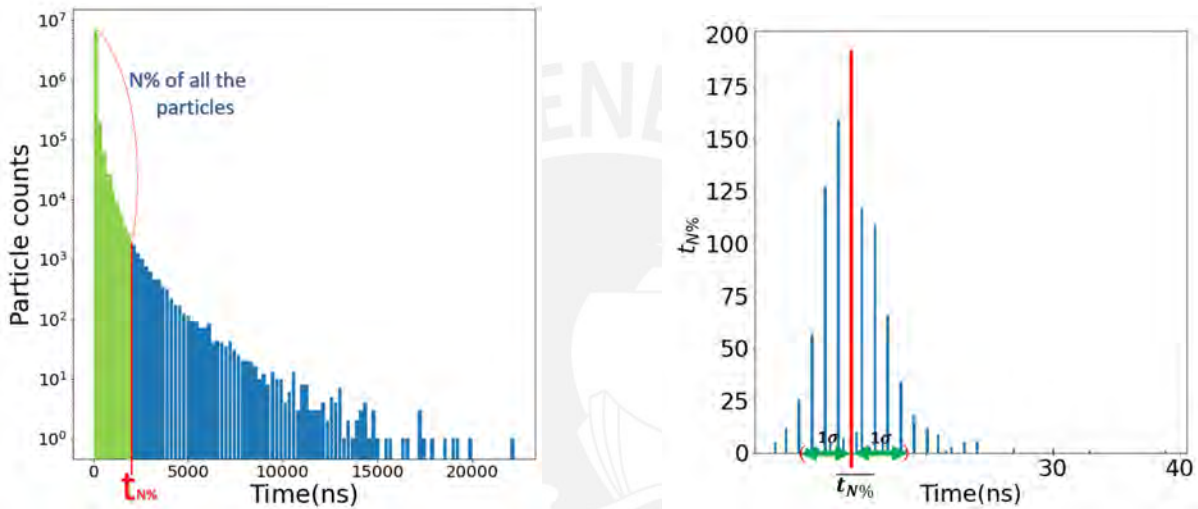
### 8.1.1 Quantiles of the Temporal Distribution

The study was premised on constructing spatial variables (taking different rings) and temporal variables (taking a characteristic time).

$t_{N\%}$  is defined as the time elapsed from when the first particle impacts the surface of the tanks until the time when N% of the total particles impact. As seen in Fig.8.2a, where N=25 is used for a gamma event at 100 TeV, after 25% of the particles have impacted the detector tanks, the time  $t_{N=25\%}$  is defined. Naturally, the N% quantile of the temporal distribution is being calculated. This characteristic time is studied in different sectors in the form of rings, as previously detailed (rings of 50 m difference in radii). The idea is to analyze  $t_{N\%}$  for various values of N = 5 - 95,

## CHAPTER 8. AIR SHOWERS TEMPORAL DISTRIBUTION

not taking the minimum value because it will be zero for both due to the scale that was made, nor the maximum value due to the stochastic nature of the secondary particle production process. The thousand simulations conducted for each type of event generate a list with a thousand  $t_{N\%}$  values for each ring and energy analyzed. The average ( $\overline{t_{N\%}}$ ) of this list is chosen as representative for each value of N%, type of event, ring, and energy. The error will be taken as  $1\sigma$  (one standard deviation) from the list, a scheme of which can be seen in Fig.8.2b, where the average  $\overline{t_{N\%}}$  is bounded by its standard deviations.



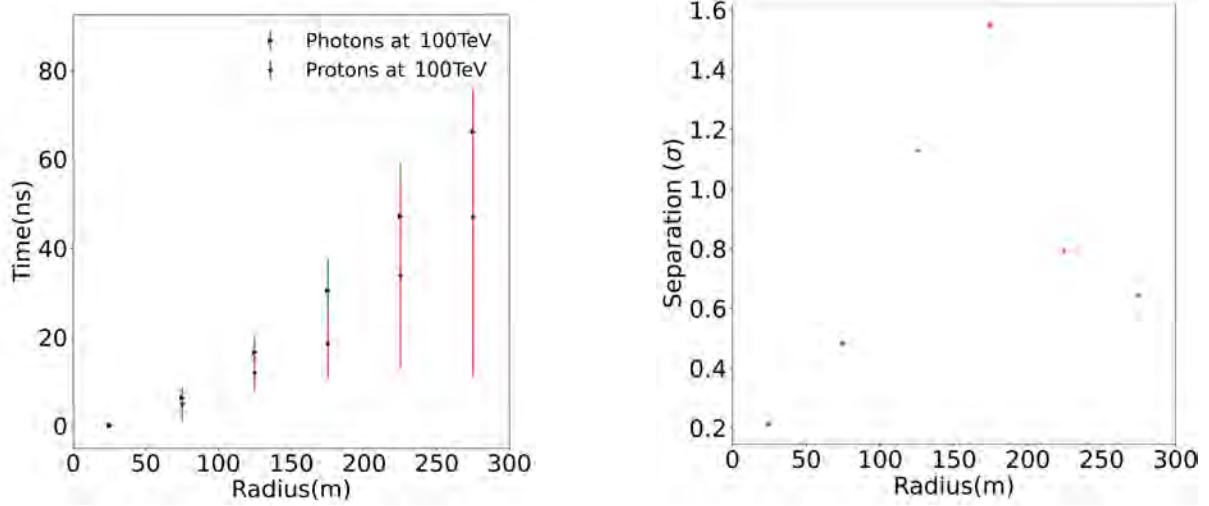
(a) Distribution of  $Time(ns)$  for  $N=25\%$  in a gamma event at 100 TeV. The bins representing  $N=25\%$  of the total secondary particles impacting the detector tanks at time  $t_{N=25\%}$  are colored green.

(b) Distribution of  $t_{N=25\%}$  in a gamma event at 100 TeV for 1000 simulated showers. The average time  $t_{N=25\%}$  is marked in red, and at the bottom the  $1\sigma$  error (one standard deviation).

**Figure 8.2:** Distributions of quantiles of the Temporal Distribution ( $t_{N\%}$ )

The premise of this research is that the  $t_{N\%}$  of hadronic and gamma events are sufficiently "separated" to serve as a variable distinguishing between both types of events at different energies. Since different values of N% can be used at different energies, to exemplify and study the nature, trends, and other aspects of these variables,  $t_{25\%}$  at the specific energy of 100 TeV will be used. The "separation" of  $t_{25\%}$  for each of the rings under analysis between each type of event can be seen in Fig.8.3a, where  $t_{25\%}$  increases as the radii of the rings increase and so does its dispersion. Furthermore, the dispersion of the hadronic events is higher and increases more rapidly than that of the gamma events.

## CHAPTER 8. AIR SHOWERS TEMPORAL DISTRIBUTION



(a) Time  $t_{25\%}$  in each ring of 50 m difference in radii for gamma and hadron events at 100 TeV

(b) Separation of  $t_{25\%}$  in terms of error in each ring of 50 m difference in radii at 100 TeV

**Figure 8.3:** Gamma-Hadron separation using  $t_{25\%}$  at 100 TeV in SWGO

To quantify the separation of  $t_{25\%}$ , Cohen's  $d$ , as previously described, will be used:

$$d = \frac{|\bar{t}_{hadron} - \bar{t}_{gamma}|}{s} \quad (8.1)$$

As in the case of muons detailed in Chapter 6, since the number of events is 1000 for both primary particles, Cohen's  $d$  simplifies to:

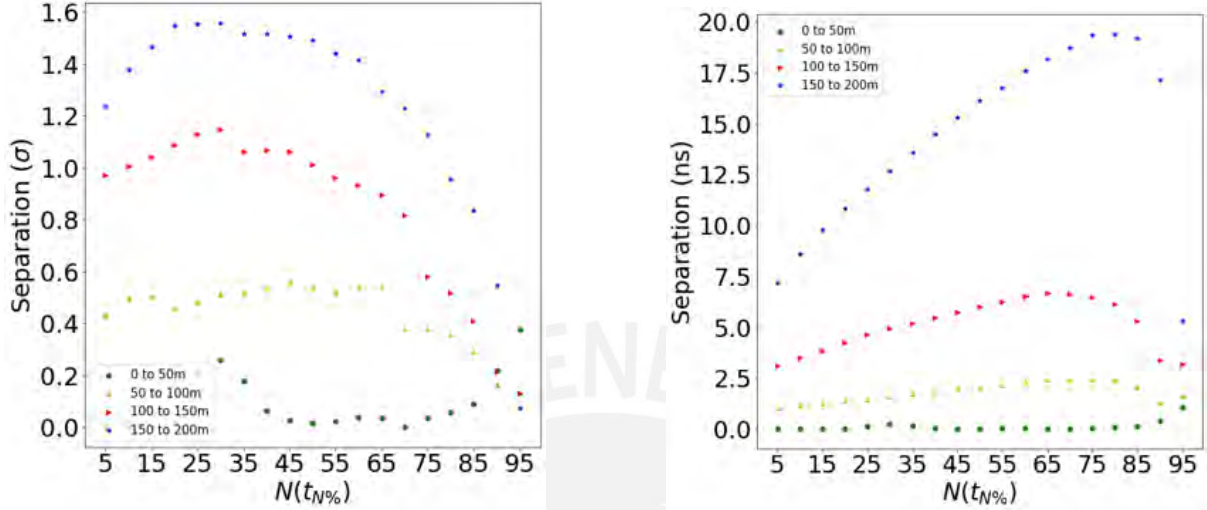
$$d = \frac{|\bar{t}_{hadron} - \bar{t}_{gamma}|}{\sqrt{\sigma_{hadron}^2 + \sigma_{gamma}^2}} \quad (8.2)$$

The values of Cohen's  $d$  (separations in terms of  $\sigma$ ) for each ring can be visualized in Fig. 8.3b, where the separation values are different for each ring. It is evident that there is a peak at the radii around 150m which suggests that in this range the optimal distance for separation is found. However, it is necessary to review the different percentiles and energies in order to corroborate this evidence or identify better candidates. Therefore, a more detailed search for the optimal value of N% and ring for gamma-hadron separation is required.

The search for the optimal gamma-hadron separator will encompass sweeps of N% from 5% to 95% across the different rings analyzed at the specific energy of 100 TeV (subsequently covering other energies of interest). For this, the same algorithm as in the example of  $t_{25\%}$  was implemented, but now iterating as many times as necessary to cover all quantiles (in 5% increments). The results of Cohen's  $d$  with different values of N% in the different rings are shown in Fig.8.4a. The best separations are found in the rings farthest away and among the first

## CHAPTER 8. AIR SHOWERS TEMPORAL DISTRIBUTION

quantiles at this energy. However, it is important to emphasize that the rings farthest from the center of the shower (core) have very low statistics compared to the inner rings and, therefore, it is better to use the inner rings (in the range from 0 to 150 m).



(a) Separation in terms of error ( $\sigma$ ) for different rings and  $N\%$  values (between 5% and 95%) at 100 TeV

(b) Difference between means ( $|\bar{t}_{hadron} - \bar{t}_{gamma}|$ ) for different rings and  $N\%$  values (between 5% and 95%) at 100 TeV

**Figure 8.4:** Gamma-Hadron Separation at 100TeV in SWGO to different  $t_{N\%}$  and rings.

On the other hand, the difference between means  $|\bar{t}_{hadron} - \bar{t}_{gamma}|$  for each  $N\%$  and analyzed ring can be observed in Fig.8.4b. As expected, the differences in means increase as the radius increases. In addition, for most cases, these differences increase as  $N\%$  increases. It is worth mentioning that the differences for the rings from 100 to 150 m and from 150 to 200 m are all greater than 2 ns, the minimum resolution required by Hamamatsu brand photomultiplier tubes (PMTs) to differentiate between one detected particle and another [67]. However, to complement this study, it is necessary to consider the time it takes to interact with the tank (and the water inside) by implementing simulations in AERIE, the SWGO collaboration simulator that is based on the Geant4 package to emulate the response of the detector tanks.

The results are not yet conclusive, although there is an apparent trend that the best candidates for gamma-hadron separator are found in the rings from 100 to 150 m and 150 to 200 m and in the quantiles between 10% to 30%. It is still necessary to corroborate these trends at different energies.

## 8.2 Candidates for Temporal Gamma Hadron Separation

In this section, the time quantiles  $t_{N\%}$  in the different rings will be analyzed in search of a trend for the optimal gamma-hadron separator at each energy level analyzed from 1 to 100 TeV. Various rings will be discarded, and some adjustments will be made until a separator that works for all energies is found.

### 8.2.1 Limiting the Optimal Rings

Fig.8.5 shows graphs for the 6 analyzed rings, where the color axis represents the value of the separation in terms of  $\sigma$ , the horizontal axis contains each of the analyzed energies (in logarithmic scale of TeV) and the vertical axis the time quantiles  $t_{N\%}$ . To begin with, the values in the 0 to 50 m ring are too low, this is because in this sector the particles arrive almost all at the same time, and therefore, the separation is very poor. Based on this argument, the 0 to 50 m ring will be rejected.

On the other hand, the outer rings from 150 to 200 m, 200 to 250 m, and 250 to 300 m will be rejected due to the low statistics. It must be taken into account that this argument is given since the area covered by SWGO in these rings is 5%. Apparently, in these sectors, there are greater separations than the inner rings. However, when the differentiation test between gamma and hadronic events is performed, some events will not be distinguished well due to the low number of particles in these rings. After this filter, two tentative rings are obtained as best candidates for gamma-hadron separation: 50 to 100 m and 100 to 150 m.

### 8.2.2 Searching for Time Quantile Trends in Rings

Initially, patterns were sought with the points of greatest separation for each energy, observing a slight trend. However, it was reviewed whether there was a smoother but more pronounced trend with the three points of greatest separation (see Fig.8.6). Such a smooth trend was not found among these points (colored in red), leading to the conduct of a different type of search. As a second search for patterns, the points with the greatest separation for both rings at all energies under analysis were re-examined. To start, a linear fit is made using an error for each point of  $\pm 5\%$ , because steps of 5% were used in each quantile (see Fig.8.7).



## CHAPTER 8. AIR SHOWERS TEMPORAL DISTRIBUTION

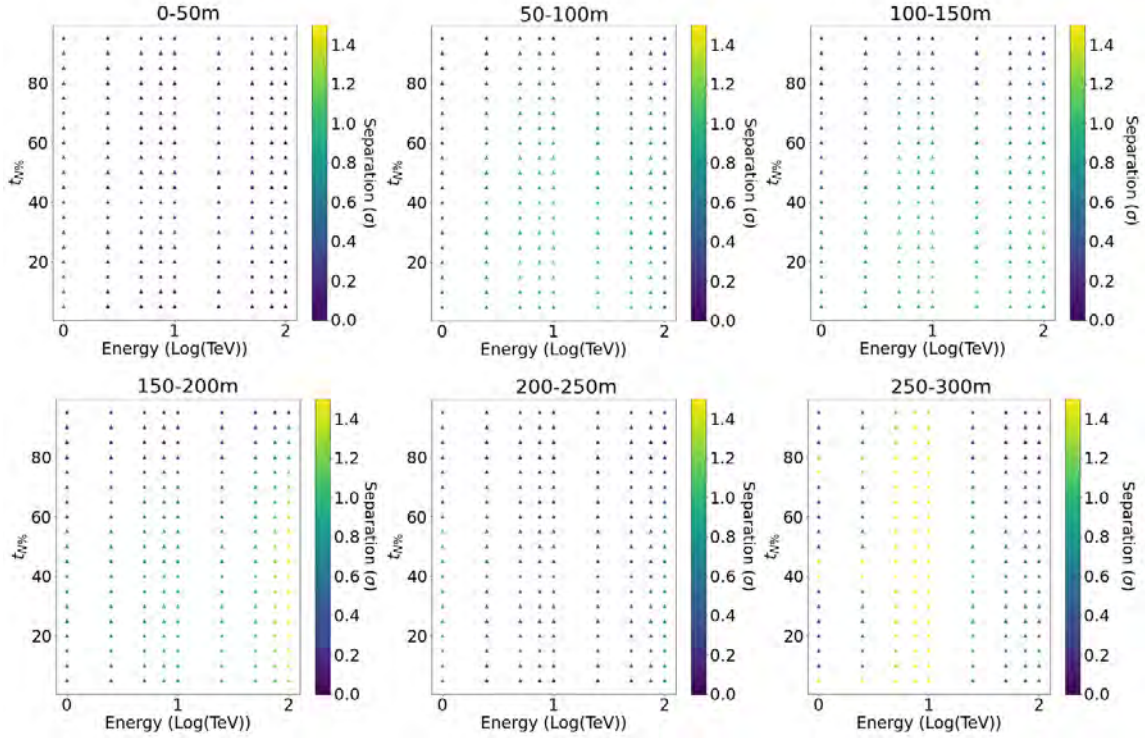


**Figure 8.5:** Gamma-Hadron Separation (based on the  $\sigma$ ) for all energies in the six analyzed rings.

The fit for the 50 to 100 m ring does not pass through all the points (especially at 100 TeV) nor through their error bars. This fit deviates significantly from the graph's values, leading to the dismissal of a linear fit in this ring, also, the value of the RMSE error committed is high (10.36). On the other hand, in the 100 to 150 m ring, although the fit does not pass through all the points, it does not deviate much from the values, and the RMSE error value is lower than in the previous graph. Furthermore, the slope of the graph is very small, so another type of fit (constant) will be made for the given points (see Fig.8.8).

The constant fits made in Fig.8.8 provide information on the quality of the fit: the reduced  $\chi^2$ , in addition to assuming an error for each point of  $\pm 5\%$ . In the graph on the left (50 to 100 m radius ring), the fit made does not pass through all the points nor their errors and deviates significantly from them, and the value of its reduced  $\chi^2$  is far from one (5.44).

On the other hand, in the 100 to 150 m ring, it behaves similarly to the linear fit (it does not pass through all the points nor their errors but is in the vicinity of the same), and its reduced  $\chi^2$  value equal to 2.44 is closer to one. Therefore the fit of  $t_{N\%=16.11\%}$  in the 100 to 150 m ring to the analyzed energies, will be accepted as correct.

From both fits, the 50 to 100 m ring is discarded due to its lack of linear or constant trend.

## CHAPTER 8. AIR SHOWERS TEMPORAL DISTRIBUTION

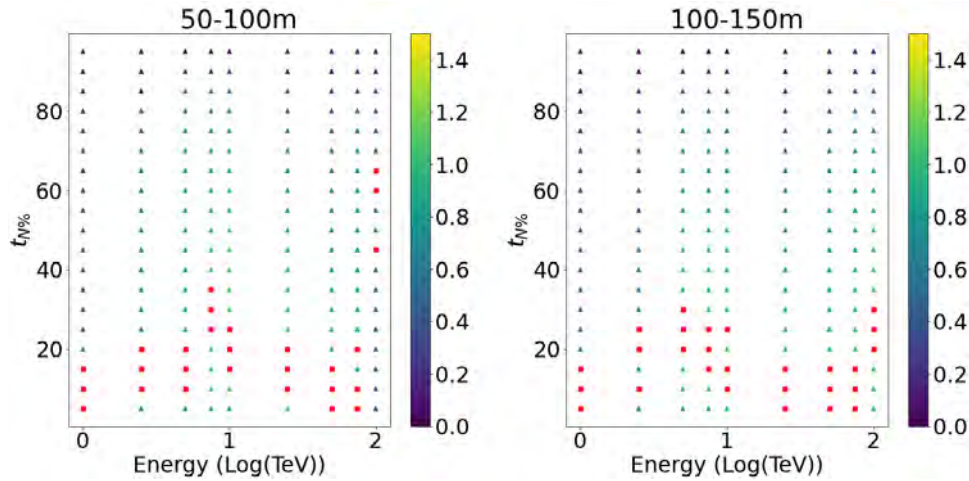


**Figure 8.6:** Location (in red) of the three points with the highest Gamma-Hadron Separation in each analyzed energy.

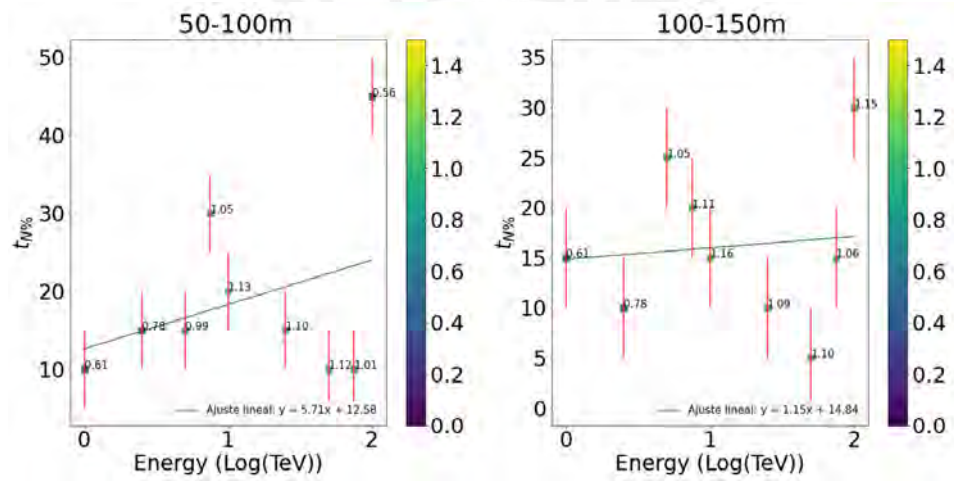


**Figure 8.7:** Linear fitting of the point with the highest Gamma-Hadron Separation in each analyzed energy.

Finally, the quantile  $t_{15\%}$  in the 100 to 150 m ring at energies in the order of 0.01 to 0.1 PeV will be used as the gamma-hadron separator in this thesis.



## CHAPTER 8. AIR SHOWERS TEMPORAL DISTRIBUTION

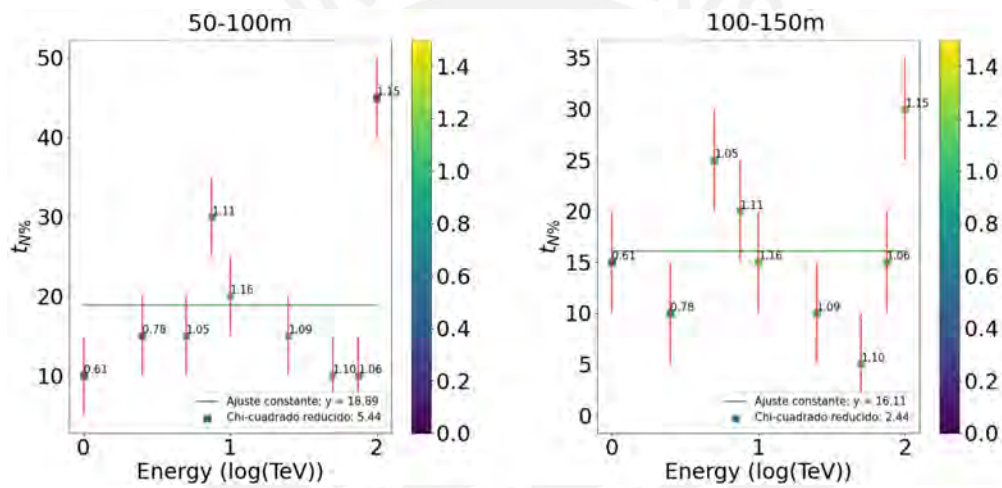


**Figure 8.8:** Constant fitting of the point with the highest Gamma-Hadron Separation in each analyzed energy with the value of its reduced chi-square.

# Chapter 9

## Evaluating the Time Gamma/Hadron Separator

In this chapter, the process of calculating and evaluating the proposed variable will be detailed. In addition, the same calculation and evaluation will be carried out for the reference variable (Muon Count) detailed in Chapter 7. It is worth mentioning that the calculation is not done with a machine learning algorithm, rather by exploring defined variables combinations.

### 9.1 Calculation and Evaluation of the Time Variable

To calculate the typical  $t_{15\%}$  variable in the 100 to 150 m ring, it was necessary to simulate new events. A total of 10,000 gamma events (primary particle: photon) and 10,000 hadronic events (primary particle: proton) were generated, of which 70% were used for the calculation of the variable in the sample and the remaining 30% for the evaluation of the variables in question.

After calculating the typical  $t_{15\%}$  variable in the 100 to 150 m ring (hereafter  $t_{15\%}$ ), different values for  $t_{15\%}$  are obtained for both gamma events and hadrons for each energy level, as well as the errors in each case. Since the distributions of  $t_{15\%}$  from gamma and hadronic air showers overlap more as the energy decreases (see Fig.9.1), it is necessary to evaluate our variable with limits that consider not only the average of the distributions but also their dispersion. Therefore, 4 types of limits are proposed:

- $t_{15\% \gamma_{min}}$ : Minimum time of the  $t_{15\%}$  distribution of gamma events.
- $t_{15\% \gamma_{max}}$ : Maximum time of the  $t_{15\%}$  distribution of gamma events.
- $t_{15\% p_{min}}$ : Minimum time of the  $t_{15\%}$  distribution of hadronic events.

## CHAPTER 9. EVALUATING THE TIME GAMMA/HADRON SEPARATOR

- $t_{15\%p_{max}}$ : Maximum time of the  $t_{15\%}$  distribution of hadronic events.

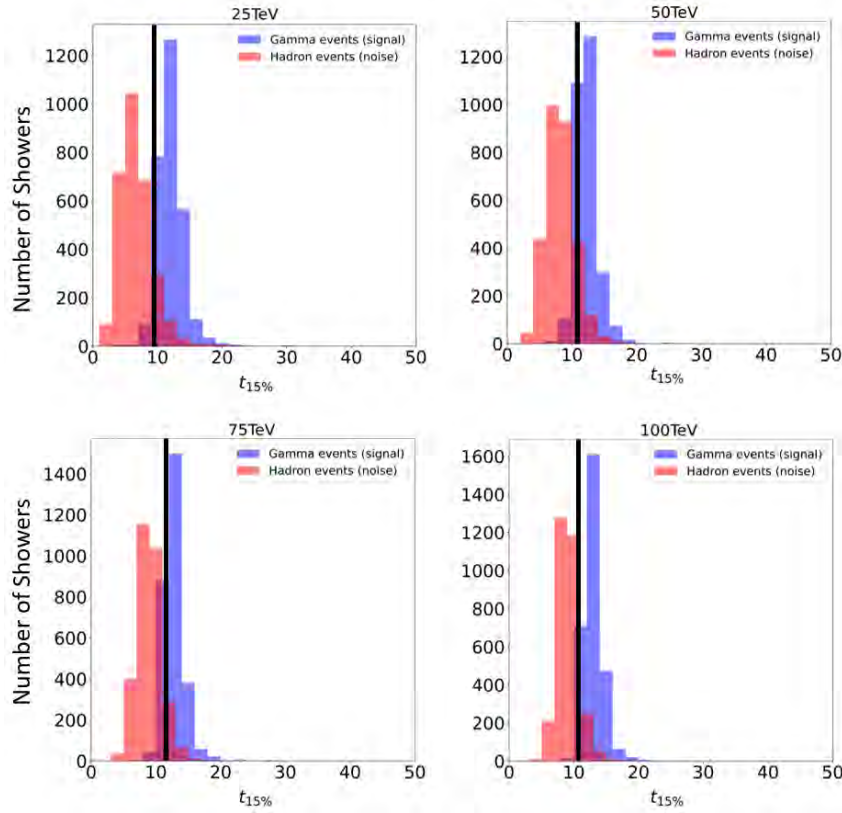


**Figure 9.1:** Distribution of  $t_{15\%}$  for gamma and hadron evaluation events (3,000 events for each type of shower) for different energies from 1 to 100 Tev. The value of the differentiator  $t_{15\%p_{max}}$  is indicated with a black line.

Given that the  $t_{15\%}$  of hadronic events are commonly lower than those of gamma events, the variables  $t_{15\%p_{min}}$  and  $t_{15\%o\gamma_{max}}$  are not useful. Therefore, the evaluation will be carried out with the other two variables.

To begin,  $t_{15\%p_{max}}$  (indicated by the black line in Fig9.1) will be used to differentiate each type of event with the following criteria: any event that has a  $t_{15\%}$  greater than the value of  $t_{15\%p_{max}}$  will be considered a gamma event, and consequently, any event with a  $t_{15\%}$  less than the value of  $t_{15\%p_{max}}$  will be a hadronic event.

After making this separation between types of events, a percentage of gamma events and another percentage of hadronic events were recognized (see Fig.9.2).

It can be observed that the background rejection has very high percentages, exceeding 89% across all energies, particularly highlighting energies between 1 and 10 TeV with values above 92%. Whereas the signal (gamma events) recognized is considerably lower at lower energies

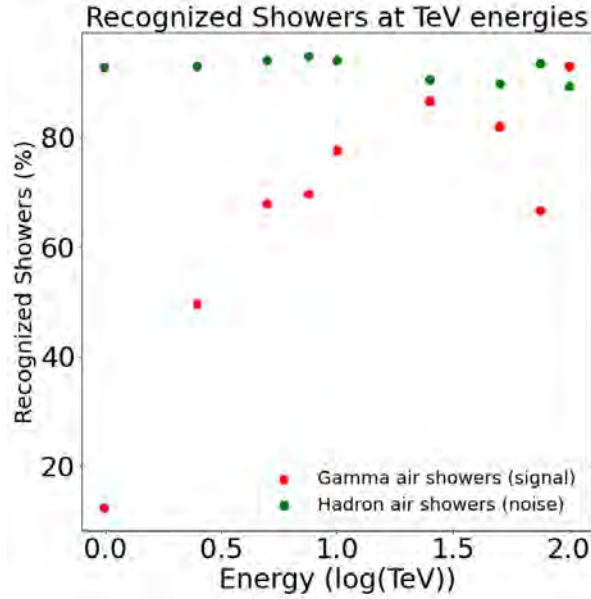


**Figure 9.2:** Percentage of signal recognized (gamma events) and noise rejected (hadronic events) using the separator  $t_{15\%p_{max}}$ .

(1 - 5 TeV) but increases above 60% at higher energies, especially noting the energy of 100 TeV with a signal recognition of 92.67%. This is due to the distributions overlapping much more at lower energies than at higher energies, which translates into an improvement in signal recognition as the energy increases.

On the other hand, using  $t_{15\%\gamma_{min}}$  as a differentiator (indicated by the black line in Fig 9.3), considering the same reasoning, if the event has a  $t_{15\%}$  greater than the value of  $t_{15\%\gamma_{min}}$ , it will be gamma, and if it is lower, it will be a hadronic event (see Fig 9.3).

The results of the evaluation are shown in Fig. 9.4, which, like in the previous case, contains the values (in percentage) of recognized signal and noise. An increase in the percentage of recognized signal can be observed. However, the background rejection shows a significant decrease.

Although the background rejection values of the separator  $t_{15\%p_{max}}$  are high, it is necessary to have a good percentage of recognized signal. Therefore, the results of the separator  $t_{15\%\gamma_{min}}$  will be used as the final results of this evaluation.

Using this variable, an average of 88% recognized signal is obtained in the analyzed energies, while 78.6% of background is rejected. These results need to be referenced with the aim of comparing their separation power with a widely used trust variable as a gamma-hadron separator

## CHAPTER 9. EVALUATING THE TIME GAMMA/HADRON SEPARATOR

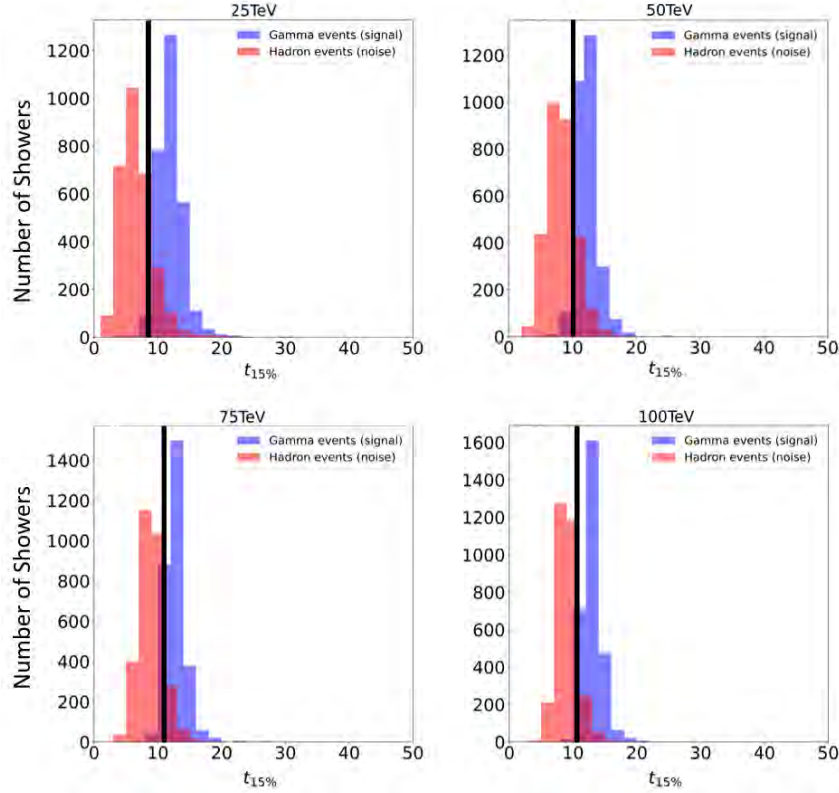


**Figure 9.3:** Distribution of  $t_{15\%}$  for gamma and hadron evaluation events (3,000 events for each type of shower). The value of the differentiator  $t_{15\%}^{\gamma_{min}}$  is indicated with a black line.

in astroparticles: the Muon Count.

### 9.1.1 Evaluating of the Muon Count Variable in SWGO

The same data were used to the calculation the Muon Count variable in the 0 to 50 m ring (hereafter  $MC$ ). From this, the respective average values of  $MC$  for gamma and hadron events were obtained for each analyzed energy, as well as the errors in each of them. Similar to the  $t_{15\%}$  variable, there will be four types of limits, of which  $MC_{\gamma_{max}}$  will be used. This differentiator is used because the amount of  $MC$  in hadronic events are significantly higher than in gamma events.

The gamma-hadron separator  $MC_{\gamma_{max}}$  is denoted with a black line in the graphs of Fig. 9.5. The separation between types of events will be done as follows: any event with a  $MC$  value higher than  $MC_{\gamma_{max}}$  will be classified as a hadronic event, and those that are lower will be classified as gamma events.

After separating the gamma events from the hadronic events, a percentage of recognized signal

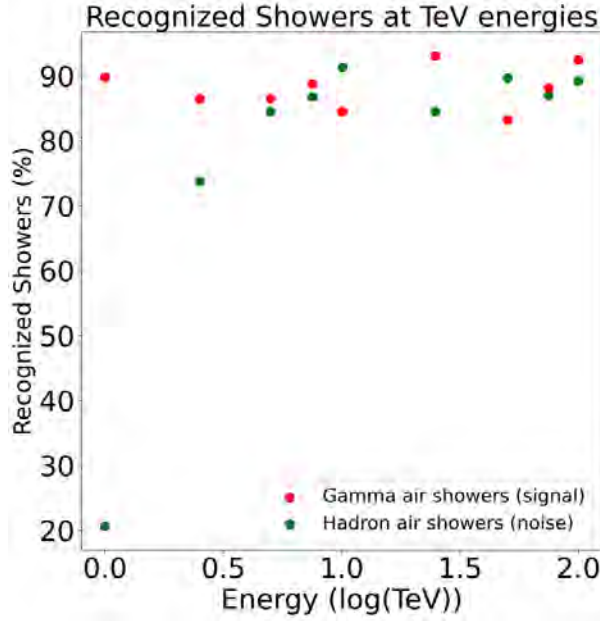


**Figure 9.4:** Percentage of recognized signal (gamma events) and rejected noise (hadronic events) using the separator  $t_{15\% \gamma_{min}}$ .

(gamma events) and rejected noise (hadronic events) was obtained (see Fig. 9.6).

The background rejection exhibits very high percentages, exceeding 96% across all energies, except at the energy of 1 TeV, which is 71.72%. This is due to the low muon count in its distribution, which has an average count very close to that of the signal, in comparison with other energies. Meanwhile, the recognized signal (gamma events) remains above 94%. The results for the muon count are high given the considerable distance between the two distributions. This, in turn, is due to the high production of muons at high energies in hadronic air showers compared to gamma air showers.

## 9.2 Results of the Comparison between the time cut separator and the Reference (MC)

The background rejection percentages using  $t_{15\% \gamma_{min}}$  as the gamma-hadron separator, averaging 78.6%, are comparable, though slightly lower than those of the  $MC_{\gamma_{max}}$  separator, which average 96.27% for the analyzed energies. This is also comparable to similar works like [64] with a background rejection of 99.97%. On the other hand, the recognized signal using  $t_{15\% \gamma_{min}}$  as the gamma-hadron separator, averaging 88%, is also comparable, though slightly lower than that of the  $MC_{\gamma_{max}}$  separator, averaging 96.21% for the analyzed energies and with the recognized

## CHAPTER 9. EVALUATING THE TIME GAMMA/HADRON SEPARATOR

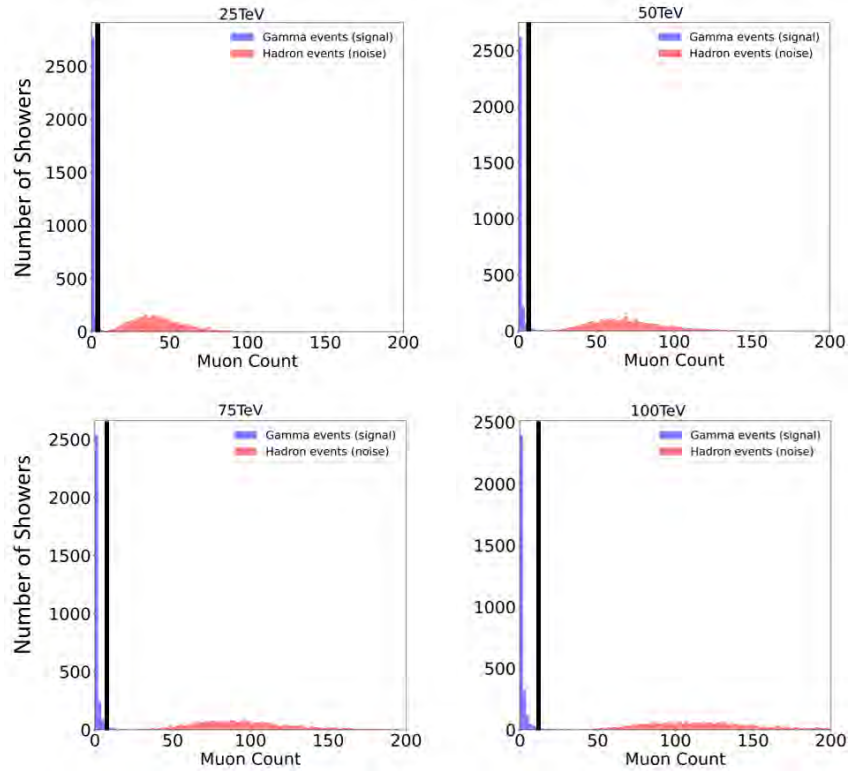


**Figure 9.5:** Distribution of  $MC$  for gamma and hadron evaluation events (3,000 events for each type of shower). The value of the differentiator  $MC_{\gamma_{max}}$  is indicated with a black line.

signal obtained in [64] averaging 92% (at energies from 30 to 300 PeV).

Ultimately, it can be inferred that the variable  $t_{15\% \gamma_{min}}$  is a gamma-hadron separator with great separation power. It is proposed for the creation of new variables derived from it, as in the case of Muon Count (from which the variables studied in Chapter 7 were developed).



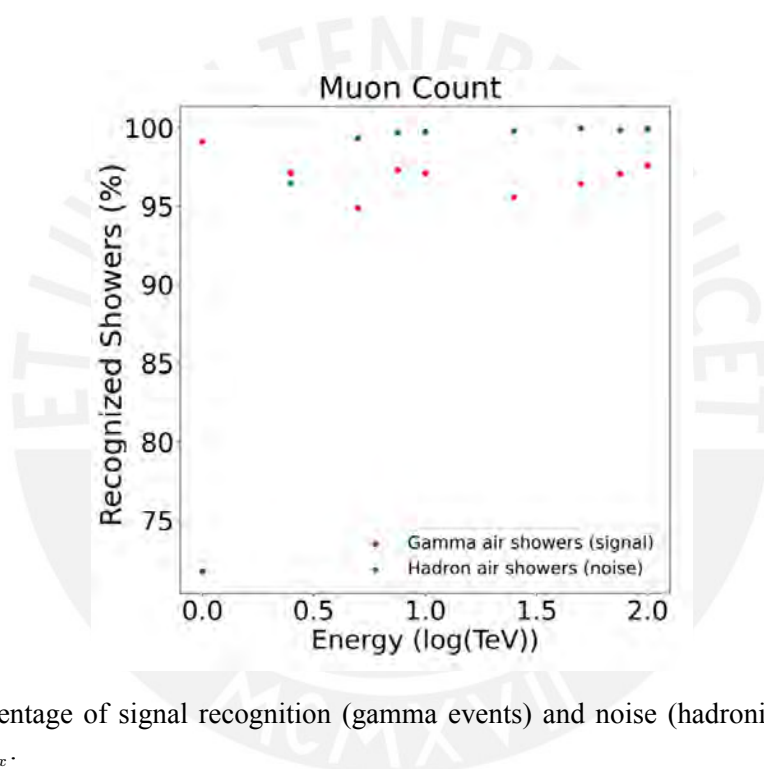


**Figure 9.6:** Percentage of signal recognition (gamma events) and noise (hadronic events) using the separator  $MC_{\gamma_{max}}$ .



# Chapter 10

## Conclusions

Gamma-ray astronomy is a very important field in astroparticle physics both for the detection and study of galactic and extra-galactic sources. SWGO will be a high-altitude gamma-ray observatory based on the technique of Cherenkov water tank arrays with a PMT inside, located in the Andes of the Southern hemisphere. It will have more than 6000 tank units distributed in two sectors (one with high and the other with low tank filling concentration, 80.7% and 5% respectively). Its sensitivity and energy range will complement experiments like HAWC, LHAASO, and CTA-South. The implementation of algorithms for the reconstruction of the properties of air showers and the incident primary particles in the atmosphere (air shower reconstruction) is of paramount interest for the proper study of the sources that generate them.

Among these methods, gamma-hadron separation is an algorithm of great importance for the detection and subsequent reconstruction of air showers, since it is necessary to distinguish between signal (gamma air showers) and noise to reject (hadron air showers). The study of new variables to implement this algorithm is necessary to advance in the improvement of signal recognition and background rejection.

In this context, after studying the distribution of the arrival time of secondary particles at the detectors, it was found that the variable analyzed in this thesis was optimal for performing the separation at the 15th percentile of the distribution ( $t_{15\%}$ ) in the 100 to 150 m ring for energies between 0.01 PeV and 0.1 PeV.

Following the training and testing conducted, the use of  $t_{15\% \gamma_{\min}}$  variable reached a recognized signal of approximately  $\gtrsim 88\%$  on average, which is sufficiently high to be comparable with the signal recognized from the reference variable Muon Count ( $MC$ ). Similarly, the background

## CHAPTER 10. CONCLUSIONS

rejection for this variable is very high ( $\gtrsim 90\%$ ) and comparable to that of the reference. From this, it can be concluded that the separator  $t_{15\% \gamma_{min}}$  is a variable that differentiates between gamma events and hadronic events with a high rate of precision.

The conducted research does not contemplate the total composition of the cosmic ray background, as only protons were simulated as primary particles for the hadronic air showers, hence the need in future studies to simulate heavy nuclei. It also does not include certain factors such as the inclination of the primary particles and the interaction of the secondary particles with the tanks and the water inside them, these being some of the limitations of the study. To consider the initial inclination, simulations could be performed for different angles and the study repeated for the typical distribution air shower inclinations. On the other hand, the interactions with the tank and water could be analyzed by implementing the AERIE simulator of the SWGO collaboration, which is based on the Geant4 package for the simulation of interactions within the tanks.

Finally, this new proposed gamma/separation variable can be integrated in more complex machine learning algorithms including other known variables to increase the sensitivity of the SWGO experiment.

# Bibliography

- [1] G. Ranganath, “Black-body radiation,” *Resonance*, vol. 13, no. 2, pp. 115–133, 2008.
- [2] L. Chengyi and M. Bo-Qiang, “LHAASO discovery of highest-energy photons towards new physics,” *Science Bulletin*, vol. 66, no. 22, pp. 2254–2256, 2021, ISSN: 2095-9273. DOI: 10.1016/j.scib.2021.07.030.
- [3] T. Gaisser *et al.*, *Cosmic Rays and Particle Physics*. Cambridge University Press, 2016.
- [4] IceCube Collaboration, “Multimessenger observations of a flaring blazar coincident with high-energy neutrino IceCube-170922A,” *Science*, vol. 361, no. 6398, eaat1378, eaat1378, Jul. 2018. DOI: 10.1126/science.aat1378. arXiv: 1807.08816 [astro-ph.HE].
- [5] Osorio, J. and others, “Actividad en rayos gamma para una muestra de blazares,” es, M.S. thesis, Universidad San Carlos de Guatemala, Guatemala, Mar. 2019.
- [6] K. Cheng *et al.*, “Origin of the Fermi Bubble,” *The Astrophysical Journal Letters*, vol. 731, no. 1, p. L17, Mar. 2011. DOI: 10.1088/2041-8205/731/1/L17.
- [7] T. Chase and F. Reddy, *NASA scientific visualization studio*, en, <https://svs.gsfc.nasa.gov/10688>, Accessed: 2024-1-23, Nov. 2010.
- [8] R. Ong, “Very high-energy gamma-ray astronomy,” *Physics Reports*, vol. 305, no. 3, pp. 93–202, 1998, ISSN: 0370-1573. DOI: [https://doi.org/10.1016/S0370-1573\(98\)00026-X](https://doi.org/10.1016/S0370-1573(98)00026-X).
- [9] C. Fromm, *Spectral Evolution In Blazars. The Case Of CTA 102*. Switzerland: Springer, 2015.
- [10] P. Schneider, *Extragalactic Astronomy And Cosmology*. Bonn - Germany: Springer, 2006, 2015.
- [11] C. Seyfert, “Nuclear Emission in Spiral Nebulae.,” vol. 97, p. 28, Jan. 1943. DOI: 10.1086/144488.
- [12] B. Peterson, *An Introduction To Active Galactic Nuclei*. Ohio: Cambridge University Press, 1997.
- [13] J. Krolik, *Active Galactic Nuclei: From The Central Black Hole To The Galactic Environment*. Princeton: Princeton University Press, 1999.
- [14] C. Urry and P. Padovani, “Unified schemes for radio-loud active galactic nuclei,” *Publications of the Astronomical Society of the Pacific*, vol. 107, no. 715, p. 803, 1995.
- [15] H. Ford *et al.*, “Narrowband HST Images of M87: Evidence for a Disk of Ionized Gas around a Massive Black Hole,” vol. 435, p. L27, Nov. 1994. DOI: 10.1086/187586.
- [16] R. Harms *et al.*, “HST FOS Spectroscopy of M87: Evidence for a Disk of Ionized Gas around a Massive Black Hole,” vol. 435, p. L35, Nov. 1994. DOI: 10.1086/187588.

## BIBLIOGRAPHY

- [17] M. Miyoshi *et al.*, “Evidence for a black hole from high rotation velocities in a sub-parsec region of NGC4258,” en, *Nature*, vol. 373, no. 6510, pp. 127–129, 1995.
- [18] H. Noda, *X-ray studies of the central engine in active galactic nuclei with Suzaku*, en. Singapur, Singapur: Springer, 2018.
- [19] K. Akiyama *et al.*, “First M87 Event Horizon Telescope results. i. the shadow of the supermassive black hole,” *The Astrophysical Journal Letters*, vol. 875, no. 1, p. L1, Apr. 2019. DOI: 10.3847/2041-8213/ab0ec7.
- [20] H. Netzer, *The Physics And Evolution Of Active Galactic Nuclei*. Ramat Aviv: Cambridge, 2013.
- [21] M. Boettcher *et al.*, Eds., *Relativistic jets from active galactic nuclei: Krawczynski: Astro jets o-bk*, en. Weinheim, Alemania: Wiley-VCH Verlag, 2012.
- [22] M. Véron-Cetty and P. Véron, “The emission line spectrum of active galactic nuclei and the unifying scheme,” *Astron. Astrophys. Rev.*, vol. 10, no. 1-2, pp. 81–133, 2000.
- [23] P. Jovanović and L. Popović, “Observational effects of strong gravity in vicinity of supermassive black holes,” *arXiv: Astrophysics*, 2008.
- [24] European Southern Observatory, *European southern observatory*, es, Accessed: 2023-10-9, Jul. 2016.
- [25] A. Quirrenbach *et al.*, “Statistics of intraday variability in extragalactic radio sources.,” vol. 258, pp. 279–284, May 1992.
- [26] C. Dermer, “Variability in blazars,” *arXiv: Astrophysics*, 1999.
- [27] J.-H. Fan *et al.*, “Variability of blazars,” *Journal of Astrophysics and Astronomy*, 2011. DOI: 10.1007/S12036-011-9037-0.
- [28] J. Gaidos *et al.*, “Extremely rapid bursts of TeV photons from the active galaxy Markarian 421,” en, *Nature*, vol. 383, no. 6598, pp. 319–320, 1996.
- [29] A. Cannon, “A comparison study of intermediate frequency BL lacs and high frequency BL lacs detected by VERITAS and fermi LAT,” es, Ph.D. dissertation, UCD School of Physics, Feb. 2011.
- [30] M. Sikora and G. Madejski, “On pair content and variability of subparsec jets in quasars,” *The Astrophysical Journal*, vol. 534, no. 1, p. 109, May 2000. DOI: 10.1086/308756.
- [31] H. o. Sol, “Two-flow model for extragalactic radio jets,” *Monthly Notices of the Royal Astronomical Society*, vol. 237, no. 2, pp. 411–429, Mar. 1989, ISSN: 0035-8711. DOI: 10.1093/mnras/237.2.411. eprint: <https://academic.oup.com/mnras/article-pdf/237/2/411/2983276/mnras237-0411.pdf>.
- [32] P. Auger *et al.*, “Extensive cosmic-ray showers,” en, *Rev. Mod. Phys.*, vol. 11, no. 3-4, pp. 288–291, 1939.
- [33] C. Grupen, *Astroparticle Physics*, 2nd ed. Cham, Switzerland: Springer Nature, 2020.
- [34] “Properties of extensive air showers,” *Acta Physica Polonica B*, vol. 35, no. 6, pp. 1787–, 2004.
- [35] W. Heitler, *The quantum theory of radiation* (International Series of Monographs on Physics). Oxford: Oxford University Press, 1936, vol. 5.
- [36] HESS collaboration, *HESS - the high energy stereoscopic system*, Accessed: 2023-11-3.

## BIBLIOGRAPHY

- [37] F. Aharonian, “Observations of the Crab nebula with HESS,” *Astronomy and Astrophysics*, vol. 457, no. 3, pp. 899–915, 2006, Cited by: 783; All Open Access, Bronze Open Access, Green Open Access. DOI: 10.1051/0004-6361:20065351.
- [38] O. Celik, “Observations of the Crab Nebula and Pulsar With VERITAS,” in *Aas/high Energy Astrophysics Division #10*, ser. AAS/High Energy Astrophysics Division, vol. 10, Mar. 2008, 12.09, p. 12.09.
- [39] E. Aliu *et al.*, “Observation of pulsed  $\gamma$ -rays above 25 GeV from the Crab pulsar with MAGIC,” *Science*, vol. 322, no. 5905, pp. 1221–1224, Nov. 2008, ISSN: 1095-9203. DOI: 10.1126/science.1164718.
- [40] CTA-LST Project, *Observations of the Crab nebula and pulsar with the large-sized telescope prototype of the Cherenkov Telescope Array*, 2023. arXiv: 2306.12960 [astro-ph.HE].
- [41] HAWC collaboration, *HAWC: the High-Altitude Water Cherenkov Observatory*, Accessed: 2023-11-4.
- [42] A. Abeysekara *et al.*, “The 2hwc HAWC observatory gamma-ray catalog,” *Astrophysical Journal*, vol. 843, no. 1, 2017, Cited by: 255; All Open Access, Green Open Access. DOI: 10.3847/1538-4357/aa7556.
- [43] Z. Cao *et al.*, *The large high altitude air shower observatory (LHAASO) science book (2021 edition)*, 2022. arXiv: 1905.02773 [astro-ph.HE].
- [44] P. Abreu *et al.*, *The southern wide-field gamma-ray observatory (SWGGO): A next-generation ground-based survey instrument for VHE gamma-ray astronomy*, 2019. arXiv: 1907.07737 [astro-ph.IM].
- [45] J. Hinton *et al.*, “The SWGO reference configuration,” 2020, Internal Research Report.
- [46] R. Conceição *et al.*, “Detector unit and array configurations for M5,” 2022, Internal Research Report.
- [47] A. Albert *et al.*, *Science case for a wide field-of-view very-high-energy gamma-ray observatory in the southern hemisphere*, 2019. arXiv: 1902.08429 [astro-ph.HE].
- [48] S. Abdollahi *et al.*, “Fermi Large Area Telescope Fourth Source Catalog,” Mar. 2020. DOI: 10.3847/1538-4365/ab6bcb.
- [49] J. Bellido, “Site evaluation document v1.4, site: Imata,” SWGO, Tech. Rep., 2021.
- [50] J. Bellido, “Site evaluation document v1.4, site: Yanque,” SWGO, Tech. Rep., 2021.
- [51] J. Bellido, “Site Evaluation Document V1.4, Site: Sibinacocha (includes Sibinacocha, Cochauma, Cochachaca Lakes),” SWGO, Tech. Rep., 2021.
- [52] P. Miranda, “Site Evaluation Document V1.4, Site: chacaltaya Plateau (cerro Estuqueria),” SWGO, Tech. Rep., 2021.
- [53] Astronomical Park, Atacama, “Site Evaluation Document V1.4, Site: Pajonales,” SWGO, Tech. Rep., 2021.
- [54] Astronomical Park, Atacama, “Site Evaluation Document V1.4, Site: Pampa La Bola,” SWGO, Tech. Rep., 2021.
- [55] A. Rovero, “Site evaluation document v1.4,” SWGO, Tech. Rep., 2021.
- [56] A. Rovero, “Site evaluation document v1.4,” SWGO, Tech. Rep., 2021.
- [57] D. Heck *et al.*, *CORSIKA: a Monte Carlo code to simulate extensive air showers*. 1998.

## BIBLIOGRAPHY

- [58] H. Ziegfried, “Cosmic ray observations at the tev scale with the HAWC observatory,” Ph.D. dissertation, Apr. 2017.
- [59] J. Vikas *et al.*, “Reconstruction and analysis of highest energy  $\gamma$ -rays and its application to pulsar wind nebulae,” Ph.D. dissertation, Jan. 2019.
- [60] J. Vikas *et al.*, “A template-based  $\gamma$ -ray reconstruction method for air shower arrays,” *Journal of Cosmology and Astroparticle Physics*, vol. 2019, no. 01, p. 012, Jan. 2019. DOI: 10.1088/1475-7516/2019/01/012.
- [61] T. Capistrán *et al.*, “Use of machine learning for gamma/hadron separation with HAWC,” *arXiv: High Energy Astrophysical Phenomena*, 2021.
- [62] L. Hedges *et al.*, *Statistical Methods for Meta-Analysis*. Orlando: Academic Press Books, 1985, pp. 108–138.
- [63] R. Conceicao *et al.*, “Muon identification in a compact single-layered water Cherenkov detector and gamma/hadron discrimination using machine learning techniques,” *European Physical Journal C*, Jun. 2021. DOI: 10.1140/epjc/s10052-021-09312-4.
- [64] N. Gonzalez *et al.*, “A muon-based observable to detect photons at ultra-high energies,” *PoS*, 2020. DOI: 10.22323/1.358.0271.
- [65] T. Capistrán *et al.*, “gamma/hadron Separation In HAWC Using Neural Networks,” in *Ground-based And Airborne Instrumentation For Astronomy VI*, C. Evans *et al.*, Eds., International Society for Optics and Photonics, vol. 9908, SPIE, 2016, p. 990 845. DOI: 10.1117/12.2232041.
- [66] R. Alfaro *et al.*, “Gamma/hadron separation with the HAWC observatory,” *Nuclear Instruments and Methods in Physics Research Section A: Accelerators, Spectrometers, Detectors and Associated Equipment*, vol. 1039, p. 166 984, Sep. 2022, ISSN: 0168-9002. DOI: 10.1016/j.nima.2022.166984.
- [67] Hamamatsu Photonics K.K, *Technical sheet photomultiplier tube R1924a-700/r1924p-700*, Hamamatsu, Photonics K.K., 2022, Accessed: Aug. 23, 2023.